NASA CONTRACTOR REPORT

NASA CR-2843

NASA CR-2843

MEASUREMENT OF BLAST WAVES FROM BURSTING PRESSURIZED FRANGIBLE SPHERES

E. D. Esparza and W. E. Baker

Prepared by
SOUTHWEST RESEARCH INSTITUTE
San Antonio, Texas 78284
for Lewis Research Center

NATIONAL AERONAUTICS AND SPACE ADMINISTRATION • WASHINGTON, D. C. • MAY 1977

Page intentionally left blank

1. Report No.	2. Government Accession No.	3. Recipient's Catalog No.
NASA CR-2843		

4. Title and Subtitle	5. Report Date
MEASUREMENT OF BLAST WAVES FROM BURSTING PRESSURIZED FRANGIBLE SPHERES	May 1977
	6. Performing Organization Code

7. Author(s)	8. Performing Organization Report No.
E. D. Esparza and W. E. Baker	SwRI-02-4306
	10. Work Unit No.

9. Performing Organization Name and Address	11. Contract or Grant No.
Southwest Research Institute P.O. Drawer 28510 San Antonio, Texas 78284	NSG 3008
	13. Type of Report and Period Covered
12. Sponsoring Agency Name and Address	Contractor Report
National Aeronautics and Space Administration Washington, D.C. 20546	14. Sponsoring Agency Code

15. Supplementary Notes

Final Report. Project Managers, Robert D. Siewert and Paul M. Ordin, Space Propulsion and Power Division, NASA Lewis Research Center, Cleveland, Ohio 44135

16. Abstract

Small-scale experiments were conducted to obtain data on incident overpressure at various distances from bursting pressurized spheres. Complete time histories of blast overpressure generated by rupturing glass spheres under high internal pressure were obtained using eight side-on pressure transducers. A scaling law is presented, and its nondimensional parameters are used to compare peak overpressures, arrival times, impulses, and durations for different initial conditions and sizes of blast source. The nondimensional data are also compared, whenever possible, with results of theoretical calculations and compiled data for Pentolite high-explosive. The scaled data are quite repeatable and show significant differences from blast waves generated by condensed high-explosives.

17. Key Words (Suggested by Author(s))		18. Distribution Statement
Blast waves	Non-ideal explosions	Unclassified - unlimited
Gas bursts	Blast scaling	STAR category 28
Experimental data		

19. Security Classif. (of this report)	20. Security Classif. (of this page)	21. No. of Pages	22. Price*
Unclassified	Unclassified	53	A04

* For sale by the National Technical Information Service, Springfield, Virginia 22161

Page intentionally left blank

TABLE OF CONTENTS

SUMMARY

Small-scale experiments were conducted to obtain data on incident overpressure at various distances from bursting pressurized spheres. Glass spheres under high internal gas pressure were ruptured by a striker and complete time histories of overpressure obtained with an array of eight side-on pressure transducers. High-speed cinematography was used in some tests to observe sphere breakup and obtain velocities of glass fragments. The reduced data presented herein include peak overpressures, arrival times, impulses, and durations which are scaled in accordance with a model law for non-ideal explosions. The nondimensional data are compared, whenever possible, with results of theoretical calculations and compiled data for Pentolite high-explosive. The scaled data are quite repeatable and show notable differences from blast waves generated by condensed high-explosives. Basic differences are lower initial overpressure, longer positive phase duration, a much larger negative phase, and a strong second shock. Such differences from TNT or point source explosions can significantly alter the blast loading from that previously used because they have been ignored. This could substantially modify the damage predictions based on "TNT equivalence".

I. INTRODUCTION

When thin-walled gas pressure vessels burst because they are subjected to excess pressure or are flawed, the sudden release of pressure can generate damaging blast waves in the surrounding air. A number of theoretical studies of the blast waves generated by this type of energy release have been conducted [1-4] and are being conducted, but very few careful experiments have been performed for verification of the theoretical predictions. The only prior sources of data we have found are fourteen tests with pressurized glass spheres ruptured by a striker by Boyer, et al [5], and five tests of bursting, thin-walled metal vessels by Pittman [6]. Only optical (shadowgraph and streak schlieren) instrumentation was employed by Boyer, et al, but Pittman measured over-pressure time histories at several distances along three radial lines from each tank center.

The work reported here is primarily experimental and is intended to provide a source of data for blast waves from well-controlled experiments on bursting gas pressure spheres. The blast sources and method of initiation were similar to that employed by Boyer, et al [5], but time histories of side-on pressures were measured at various radii, rather than simple trajectories of shock fronts. All tests were conducted at small scale, using compressed air and argon as the test gases. A scaling law was developed to compare data for different initial conditions and size of blast source. Reduced data are presented in terms of dimensionless parameters from the scaling law.

The scaled data are quite repeatable, but show significant differences from blast waves generated by condensed explosives such as TNT. The report describes the test arrangement and experiments and gives scaled data for blast overpressures, impulses, and other measured parameters. The results are discussed and additional experimental and theoretical work is recommended.

II. SCALING LAW

A model analysis of blast waves generated by pressure spheres burst in "free air", i.e., away from the ground surface, was developed. The blast source is idealized as a sphere of gas at an initial pressure higher than atmospheric which is suddenly released from a massless spherical shell at time zero. The effects on the blast wave of the pressure container or the fragments from the container are not considered in the analysis. Scaling laws for the subsequent formation and transmission of the blast waves through the atmosphere were derived.

Identification of the pertinent physical parameters and the grouping of these parameters to describe the blast source, ambient air conditions and characteristics of the blast wave are presented in Appendix A. Some of the dimensionless parameters are combined and some reduced by applying physical restrictions such as considering perfect gas behavior throughout the system.

Also, in the tests only air and argon were used as pressurized gases in the blast wave source. The differences in values of ratios of specific heat for the two gases are minor (air - 1.4; argon - 1.667) and permitted the use of a reduced form of the scaling law. These are discussed in Appendix A. The condensed form of the scaled blast wave properties and scaled parameters used is:

$$\left.\begin{aligned} \bar{P}_s &= \left(\frac{P_s}{p_a}\right) \\ \bar{t}_a &= \left(\frac{t_a a_a p_a^{1/3}}{E^{1/3}}\right) \\ \bar{T} &= \left(\frac{T a_a p_a^{1/3}}{E^{1/3}}\right) \\ \bar{I}_s &= \left(\frac{I_s a_a}{p_a^{2/3} E^{1/3}}\right) \end{aligned}\right\} = f_i\left[\left(\frac{p_1}{p_a}\right), \frac{R p_a^{1/3}}{E^{1/3}}\right]$$

where

p_a = ambient pressure (absolute)

a_a = ambient sound velocity

P_s = peak side-on overpressure

t_a = arrival time of the peak overpressure

T = duration of the overpressure

I_s = specific impulse

R = radius of blast wave (standoff distance)

p_1 = internal absolute pressure of sphere

E = internal energy in the sphere

and $\bar{R} = \dfrac{R p_a^{1/3}}{E^{1/3}}$

The barred quantities indicate nondimensional quantities corresponding to the desired dimensional quantities.

III. THE EXPERIMENTS

A. General

Twenty experiments were conducted in this project using 51 and 102 mm (2 and 4 in) nominal diameter glass spheres of several different thicknesses as the blast source. Two different gases, air and argon, were used to pressurize the 51 mm (2 in) spheres with internal absolute pressures from 20.6 to 53.5 atmospheres. The 102 mm (4 in) spheres were pressurized from 12.2 to 31.8 atmospheres. Because of the lack of pressure-time data from non-ideal explosions, the general emphasis in this task was to obtain time histories of incident overpressure from pressurized spheres bursting in air at as many locations as possible per test. Also, it was desired that in each test some of the measurements be made as close to the glass sphere as was physically possible with the transducers used.

The experiments were set up in a fashion similar to those conducted by Boyer, et al [5]. The glass spheres were ruptured by a pneumatic striker while under high internal pressure. However, unlike the previous experiments, the instrumentation consisted of an array of eight side-on blast pressure transducers at various distances along three radials from the sphere's centers. In addition to the pressure measurement system, high-speed cinematography was used in some of the tests to observe sphere breakup and obtain velocities of glass fragments. The velocity data were used to obtain the energy driving the blast wave by computing the fragment kinetic energy and subtracting it from the initial energy in the compressed gas.

B. Experimental Layout

The tests were conducted in a blast chamber at SwRI as shown in Figure 1. The measuring equipment in the chamber included two aerodynamically-shaped, pencil-type blast pressure transducers and a double-wedge probe with six blast pressure transducers spaced along the upper surface. All eight of these transducers measured the side-on blast pressures generated by the bursting pressurized glass spheres. A high-speed movie camera, protected by a sheet of transparent plastic held in a wooden frame, photographed the test event. The required lighting was provided by a high intensity spotlight.

The glass spheres were blown from Pyrex glass tubing and were furnished with a neck about 51 mm (2 in) long. Two different schemes, shown in Figure 2, were used to couple the spheres to the pressurization system. For those spheres of nominal thickness less than 1.5 mm (0.060 in), a short piece of high-pressure nylon hose, 6.35 mm (0.25 in) inside diameter by about 76 mm (3 in) long, was used with hose clamps to connect the sphere to

FIGURE 1. OVERVIEW OF EXPERIMENTAL APPARATUS

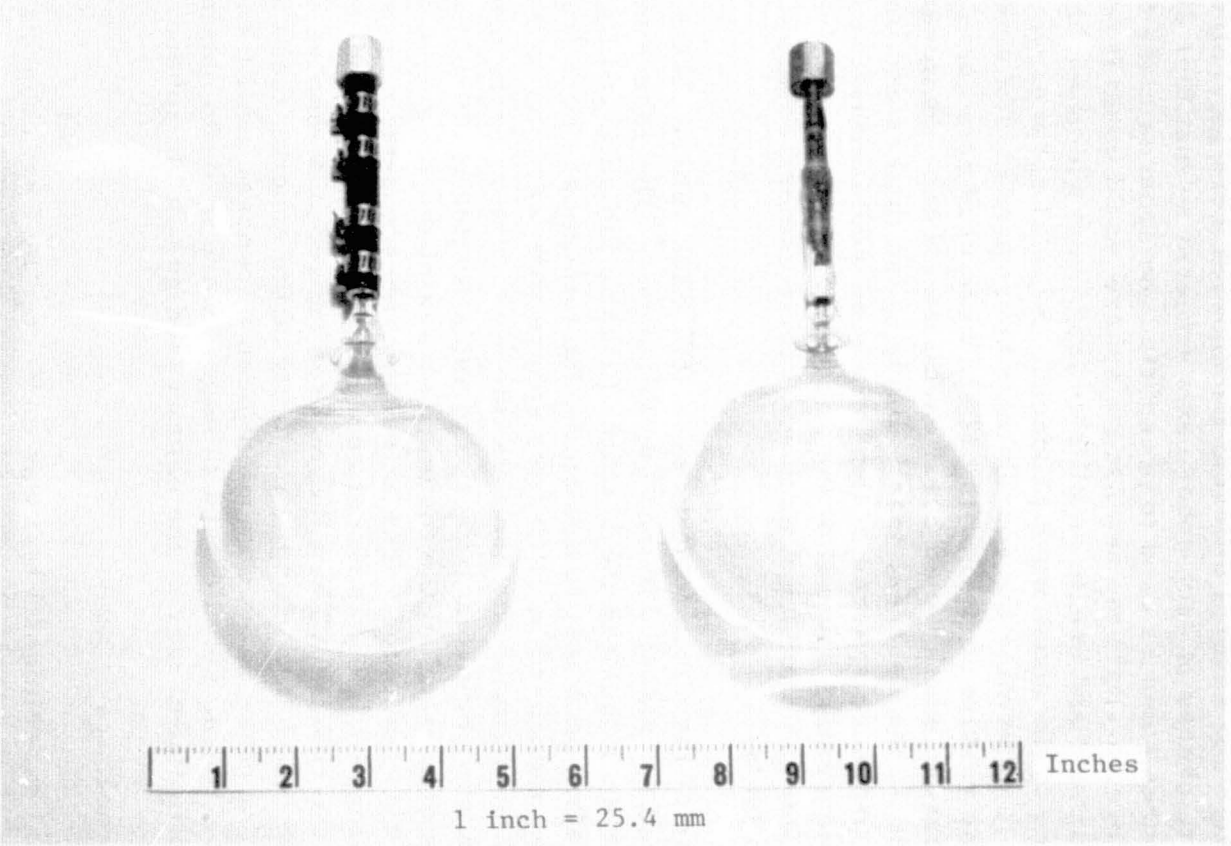

FIGURE 2. NECK CONFIGURATIONS OF GLASS SPHERES

steel tubing. For the thicker wall spheres, the inside diameter of the neck of the sphere was 6.9 mm (.27 in) and a short piece of 6.35 mm (0.25 in) steel tubing with a tubing fitting was epoxied inside the neck to connect the sphere to the rest of the pressurization system.

Two different size glass spheres of 51 and 102 mm (2 and 4 in) nominal diameter and several different thicknesses were hand blown for this project. The thickness of each sphere was selected so that four different internal pressures could be used to pressurize the spheres close to the break point. Therefore, a slight tap against the sphere would burst it relatively uniformly all around and create small size fragments which would minimize the interference to the shock wave produced. Several spheres were pressurized to destruction to determine the approximate burst pressure of each size and thickness. The results of Boyer, et al [5], were used as a guideline for estimating the pressure which would burst each size sphere. However, because of nonuniformities in the spheres, (particularly in the thicker and larger ones), the maximum pressure spheres of the same size would withstand varied significantly. Consequently, several of the spheres burst prematurely during the tests and this was the primary reason why movie camera coverage was not possible on all tests.

Because of the nonuniformity expected, each sphere tested was individually measured for mass, volume, and thickness. The sphere assembly was weighed before each test and the remains (usually the neck and its fittings) were weighed after each test to determine the total mass of the fragments. The volume was measured by filling the sphere with water up to the bottom of the neck and then emptying the contents into a graduate. Using this volume a mean diameter was computed using the formula for the volume of a sphere. With this mean diameter and the measured mass of the sphere, a mean sphere thickness was also computed. The actual thickness was also measured using ultrasonic sensors by taking several spot measurements around the sphere and averaging the results. The spheres used ranged in thickness from 0.81 to 4 mm (0.032 to 0.157 in). For the majority of the spheres these average values were very close to the computed mean thickness. All these measurements of sphere mass, volume, and thickness were made to obtain as accurately as possible the initial energy of the compressed gas in the sphere.

C. Test Procedure

A typical experimental test was conducted by first coupling a glass sphere to a remotely operated solenoid valve as shown in Figure 1. The solenoid valve was rigidly mounted onto wooden boards supported from the roof and was connected using steel tubing to high-pressure gas cylinders located in an adjacent test cell as shown in the diagram on Figure 3. A

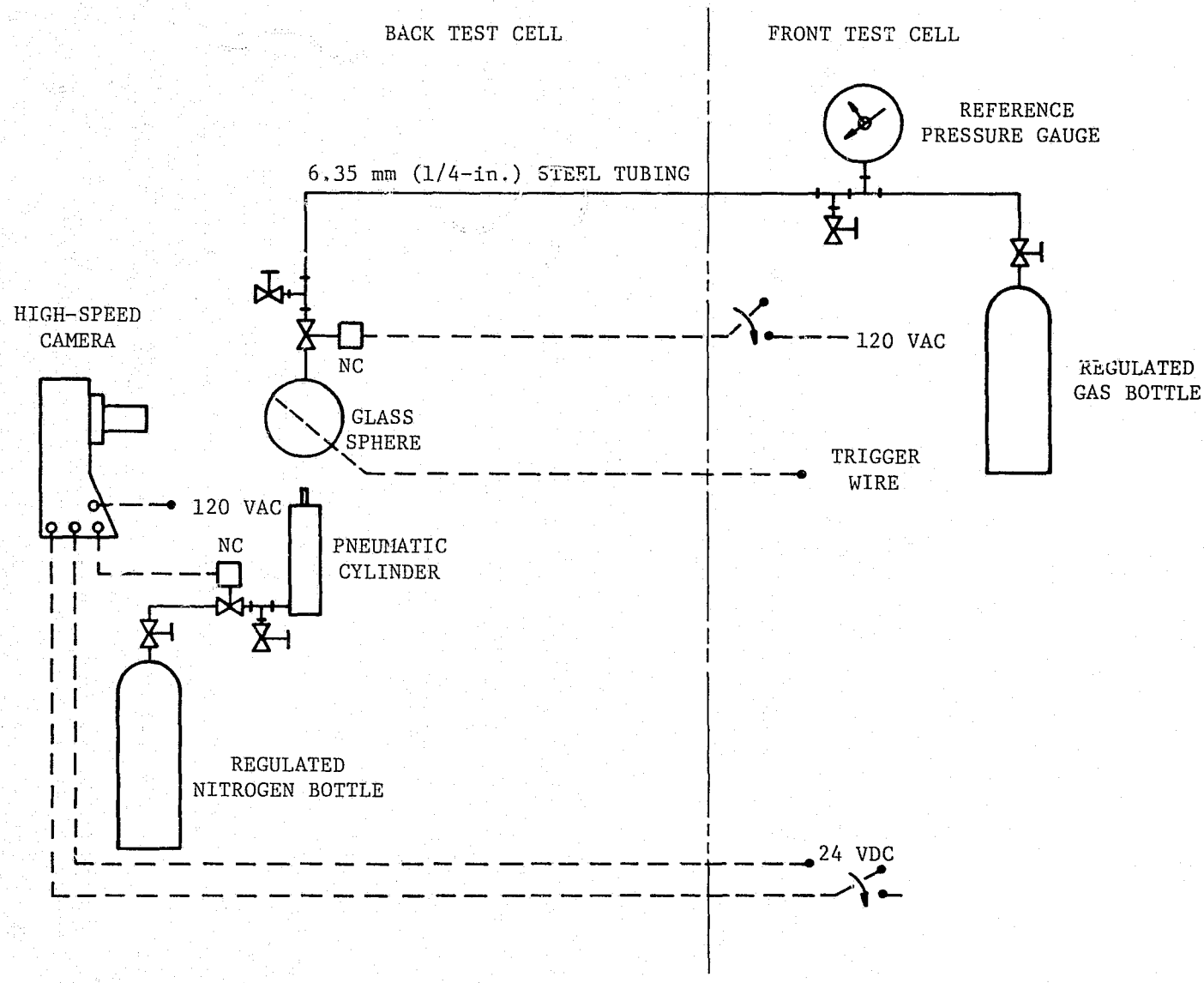

FIGURE 3. DIAGRAM OF EXPERIMENTAL SET-UP

precision bourdon-tube dial gage was used to monitor the pressure in the line (and in the sphere). By use of a "maxi-pointer", this gage also indicated the pressure at which some of the spheres burst prematurely. Two manually operated valves, one adjacent to the solenoid valve and one by the gas cylinder, provided the means of venting line pressures and, in the tests using argon, purging the sphere and tubing at low pressures.

Once the sphere was properly connected to the solenoid valve and purged, a short length of very fine wire was lightly taped around the sphere for use in a break-circuit to provide a trigger voltage for the recording instrumentation. Then the pneumatic cylinder was positioned under the sphere so that when pressurized, the striker would travel about 4 mm (0.16 in) past the bottom surface of the sphere. The cylinder was mounted on a wooden table which provided vertical height adjustment for the different sized spheres. The solenoid valve controlling the input to the pneumatic cylinder was connected to a normally open set of contacts in the high-speed camera which prevented the energizing of the solenoid by a 24 VDC supply until the camera was up to speed and ready to photograph the event. Checking to be sure that the camera contacts were in fact open and that the remote start switch for the camera was in the off position before opening the nitrogen bottle regulator connected to the pneumatic cylinder prevented any accidental breakage of the glass spheres.

The transducer holders were installed on vertical pipe stands so that vertical adjustment was possible. With the glass sphere already in place, the transducer probe point or edge was aligned along a radial through the sphere center. The three probes were placed 90° apart with the center probe opposite the movie camera. The tips of the other two probes were framed into the movie pictures to provide a known reference since the transducers were placed a measured distance from the exterior of the sphere. With the camera control connections verified to be in order, and the sphere and transducers properly installed, the camera was framed, focused, and loaded with a roll of high speed negative film (Eastman 4X) and the camera speed set a nominal 5000 frames per second. The back test cell was then evacuated and closed off.

The sphere was then pressurized from the adjacent blast cell by first energizing (opening) the remotely operated solenoid valve. The pressure in the line was very gradually increased until the desired pressure was reached. The regulator was then closed, and the gas in the line and sphere allowed to stand for several minutes and reach ambient temperature. At the same time the pressure gauge was observed to make sure there were no leaks in the system. If a drop in pressure occurred, the system was depressurized and the cause of the leaks found and corrected. The purging and pressurization

process was then repeated. Once the internal pressure was correct, the remotely controlled solenoid valve was deenergized (closed) and the tubing line vented. Prior to the pressurization process, the recording instruments were set up to record data so that even if the sphere burst prematurely, pressure data would be obtained. A "maxi-pointer" in the pressure gauge provided the indication of the burst pressure reached.

The high-speed camera and the spotlight were then turned on to begin the actual test. At a preset point of film travel, the contacts in the camera closed which energized the solenoid on the pneumatic cylinder. The cylinder was pressurized and the striker burst the sphere releasing the high-pressure gas. The bursting of the sphere broke the trigger wire which in turn triggered the pressure transducers record instrumentation. After the event, the high-speed camera was unloaded, the film processed, the pneumatic cylinder depressurized, the remains of the sphere removed and weighed, and the test cell cleaned and made ready for the next experiment.

D. Measurement Systems

Two types of measurements were made in this project: fragment velocity and side-on blast overpressures. Twelve of twenty experiments were photographed using a Redlake Hycam motion picture camera. Cinematography coverage was used to measure the fragment velocity to obtain the actual energy driving the blast wave by computing the fragment kinetic energy and subtracting it from the initial energy in the compressed gas. Eight of the tests did not have movie coverage because these spheres burst prior to reaching the desired gas pressure. Since the spheres were individually hand-blown, it was difficult for the glassblower to obtain the exact thickness specified. Furthermore, uniform thicknesses were difficult to achieve, particularly with the thicker spheres.

The field of view of the camera was composed using a 200 mm (7.9 in) zoom lens so that at least 50 to 75 mm (2 to 3 in) on either side of the glass sphere was photographed. The pressure transducer probes were used as distance references for obtaining fragment travel. A 1-kHz timing mark was imprinted on the film for time reference to obtain the actual film speed on each test.

The primary objective of this program was to obtain pressure-time data from non-ideal explosions. This was accomplished by using eight pressure transducers throughout the experimental program. Two of them were Celesco Model LC-33 piezoelectric transducers which are aerodynamic pencil-type probes specifically designed for measuring side-on blast pressures over a range of 0.69 to 3,450 kPa (0.1 to 500 psi). These two transducers have a lead-zirconate-titanate sensing element with high capacitance and charge sensitivity. The sensing element has a natural frequency greater than 67 kHz making it capable of measuring pressure transients with rise times down to about 6 μ sec. In most

cases, however, the limiting factor on transient response was the actual time required by the blast wave to travel over the length of the sensing element. This is particularly true for the experiments with the lower pressures and at the more distant measuring points where the blast wave was travelling at a lower Mach number.

The other six transducers were mounted on an aluminum double-wedge probe designed to minimize any effects on the blast waves while at the same time allowing overpressure measurements at up to six different distances from the blast source along one radial. Because this probe presented a larger target of softer material than the two stainless steel pencil-type probes, it was positioned further back to minimize fragment damage to the aluminum knife-edges. The pencil-type probes were positioned on the same horizontal plane along two radials, 90° apart and the double-wedge along a third radial also 90° apart from one of the other probes. The closest attempted measurement location placed the point of pencil-type probe at 25.4 mm (1 in) from the surface of the sphere. The sensing element on the probe was 88.9 mm (3.5 in) back from the tip so that for the 51 mm (2 in) diameter spheres measurements were made as close as 140 mm (5.5 in) to the center of the sphere, and for the 102 mm (4 in) diameter spheres, the nearest measurement was at 165 mm (6.5 in) from the center of the sphere.

The six pressure transducers used with the wedge probe are made by Susquehanna Instruments and included Model ST-2's at the first four positions and Model ST-3's at the back two locations. The ST-2 is a piezoelectric transducer with a range of 0.69 to 3,450 kPa (0.1 to 500 psi) using a 5.33 mm (0.21 in) diameter lead metaniobate sensing element having a natural frequency of 250 kHz. The ST-3 is a similar, though slightly larger, transducer with a range of 0.69 to 690 kPa (0.1 to 100 psi) using a 9.53 mm (0.375 in) diameter lead zirconate sensing ceramic having a natural frequency of 100 kHz.

All transducers were calibrated prior to testing using a hydraulic dynamic calibrator for the higher pressures and a pneumatic calibrator using a quick-vent solenoid valve for the lower pressures. The transducers were connected to SwRI-built impedance matching amplifiers consisting of a variable step capacitance input for different charge attenuation settings and into a field effect transistor circuit with very high input impedance. The output, which has a low impedance, was then amplified for driving long cable lines to the data recorder. The frequency response of this unit is about 0.1 Hz to 4 MHz. Originally, the data were to be recorded on a Wideband II, FM tape recorder which has an upper record frequency capability of 500 kHz at 3.05 m/s (120 ips). This recorder was used unsuccessfully on the first two tests because of the premature bursting of some of the spheres, and because of the very low overpressures at the further locations, very low voltage signals were produced

which were not sufficient to drive the tape recorder. Therefore, two transient digital recorders and one oscilloscope were used to record the data from the eight transducers. These instruments can handle the lower input voltage and be triggered even on premature bursts while providing sufficient frequency response for good fidelity recording. The only drawback was the compromise required in setting sweep times so that a sufficient time interval was allowed to record the first and second positive peak pressures while maintaining sufficient resolution for measuring the first positive and negative areas under the pressure-time trace to obtain the positive and negative impulses.

One transducer output was recorded on a Biomation Model 802 digital recorder as shown in Figure 4. This unit has a maximum frequency response of 500 kHz when using it at its minimum record interval of 500 μ sec full scale. The response decreases proportionally as the record interval increases since the recorder contains a fixed number of storage points. Four other transducers' outputs were recorded on a Biomation Model 1015 four channel digital recorder. Each channel on this unit has a frequency response of 25 kHz at its minimum record interval of 10 ms full scale which was the setting used throughout the test program. The other three pressure channels were recorded using a Tektronix Model R561B oscilloscope with a Model 3A74 plug-in amplifier. The frequency response of this plug-in is 133 kHz for each channel when three traces are recorded. The output of both Biomation recorders was displayed on a Tektronix Model 602 unit. All data were recorded on Polaroid film for subsequent data reduction. Very little data were recorded on the first test using the system shown in Figure 4 but this test did provide voltage level and time setting ranges so that for the remaining 17 tests, first peak overpressure was obtained on all eight channels over 95% of the time. The other blast parameters associated with the first positive and negative phase of the wave as well as the second positive peak pressure were also obtained from all eight channels of instrumentation on almost every one of these tests.

E. Data Reduction

Several blast parameters were measured and recorded in this test program. The overpressure data traces from these non-ideal explosions are quite repeatable and characterized by an initial shock overpressure, a gradual decay back to ambient, a long duration and significant negative pressure phase, and a second shock overpressure of lower amplitude than the first. Figure 5 shows several examples of the type of data recorded for both size spheres and gases used in the program. The symbols used in this figure were defined in Section II. The value of the first peak overpressure is given along with the standoff distance. The reduced data obtained from these experiments included the peak overpressures for both first and second shocks, first positive phase and negative phase impulses, times of arrival of first and second shock, and the durations of the first positive and negative phases.

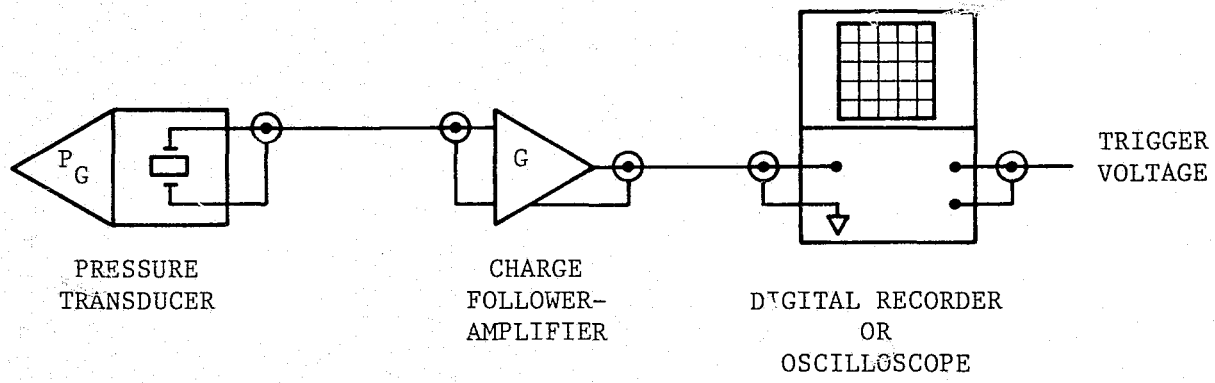

FIGURE 4. DIAGRAM OF MEASURING SYSTEM

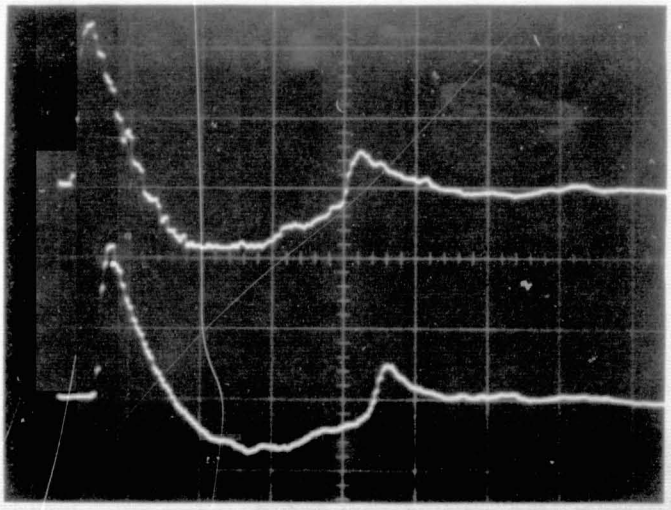

P_{s_1} = 39.6 K Pa
$\bar{P}_{s_1}$ = 0.40
R = 140 mm
$\bar{R}$ = 0.69

P_{s_1} = 33.7 K Pa
$\bar{P}_{s_1}$ = 0.34
R = 165 mm
$\bar{R}$ = 0.82

0.2 ms

TEST NO. 8, AIR
DIAMETER = 51 mm, p_1' / p_a = 52.5 atm

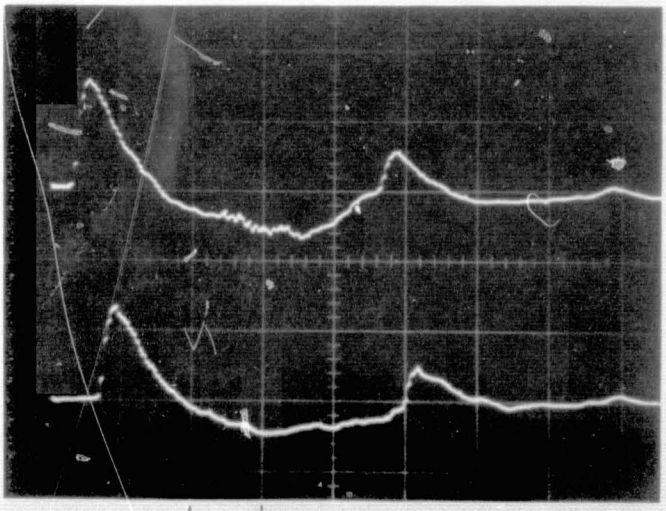

P_{s_1} = 26.4 K Pa
$\bar{P}_{s_1}$ = 0.27
R = 140 mm
$\bar{R}$ = 1.00

P_{s_1} = 20.3 K Pa
$\bar{P}_{s_1}$ = 0.21
R = 165 mm
$\bar{R}$ = 1.18

0.2 ms

TEST NO. 12, ARGON
DIAMETER = 51 mm, p_1' / p_a = 52.5 atm

FIGURE 5. EXAMPLES OF PRESSURE-TIME HISTORIES

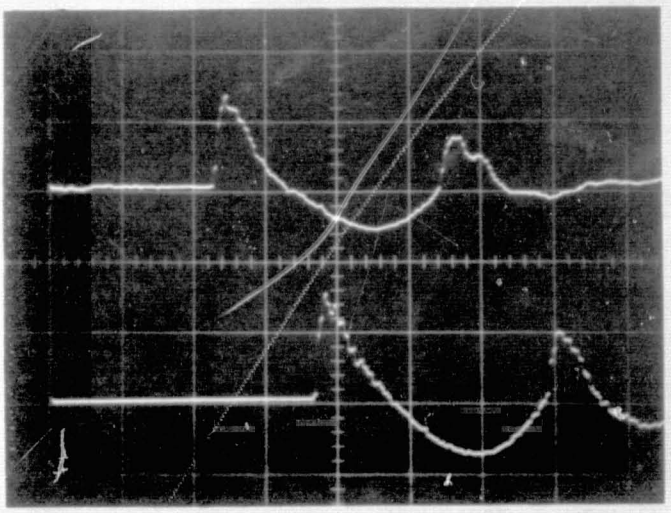

P_{S_1} = 9 K Pa
$\bar{P}_{S_1}$ = 0.092
R = 280 mm
$\bar{R}$ = 2.34

P_{S_1} = 5.6 K Pa
$\bar{P}_{S_1}$ = 0.056
R = 380 mm
$\bar{R}$ = 3.2

0.2 ms

TEST NO. 14, ARGON
DIAMETER = 51 mm, p_i'/p_a = 22 atm

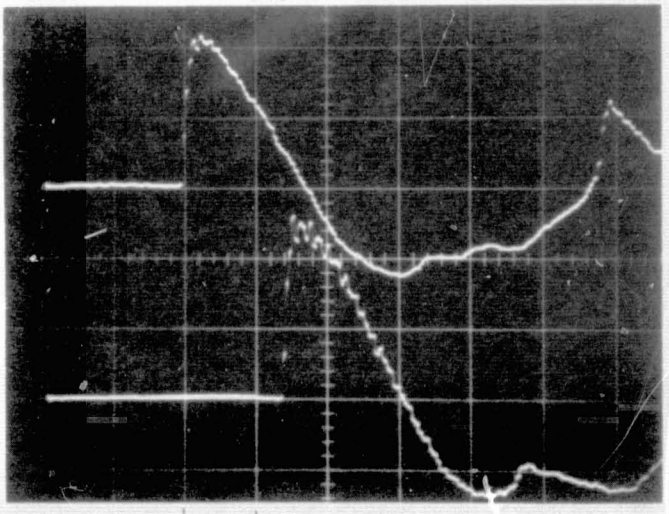

P_{S_1} = 14.7 K Pa
$\bar{P}_{S_1}$ = 0.15
R = 305 mm
$\bar{R}$ = 1.41

P_{S_1} = 9.9 K Pa
$\bar{P}_{S_1}$ = 0.1
R = 406 mm
$\bar{R}$ = 1.83

0.2 ms

TEST NO. 15, ARGON
DIAMETER = 102 mm, p_i'/p_a = 15 atm

FIGURE 5. (Cont'd.)

The Polaroid photographs were read directly to obtain the peak pressure and arrival time data. The data traces were also manually digitized, manipulated, and plotted using a Hewlett-Packard Model 9830 Calculator to obtain pressure and impulse plots with engineering units. From these plots the impulses and durations were read, and the peak pressure and arrival time data double checked. Examples of these plots reduced in size are shown in Figure 6 and 7.

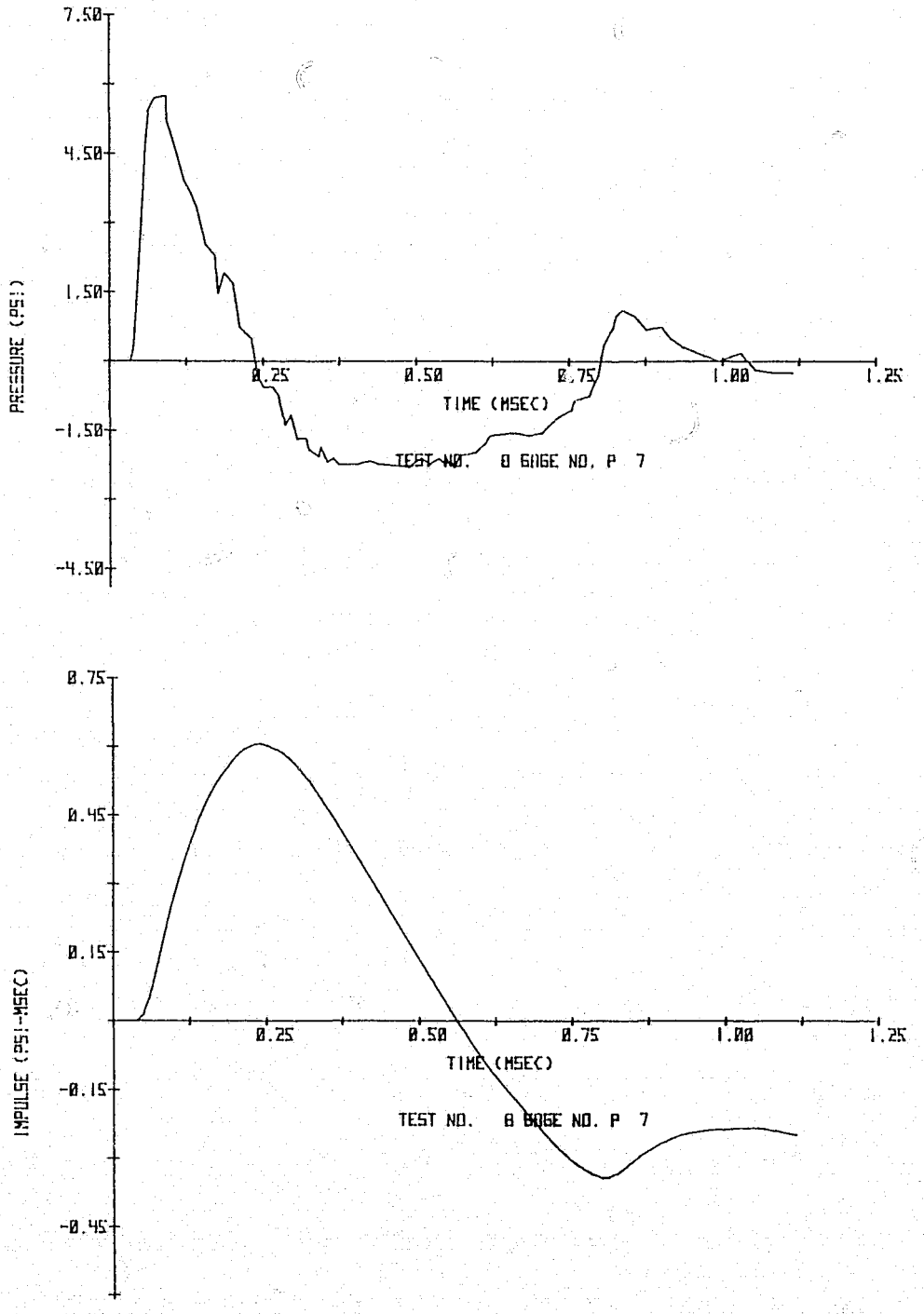

1 psi = 6.895 kPa

FIGURE 6. PRESSURE AND IMPULSE MEASURED AT $\overline{R}$ = 0.69 FROM 51 mm SPHERE PRESSURIZED WITH AIR TO 52.5 ATMOSPHERES

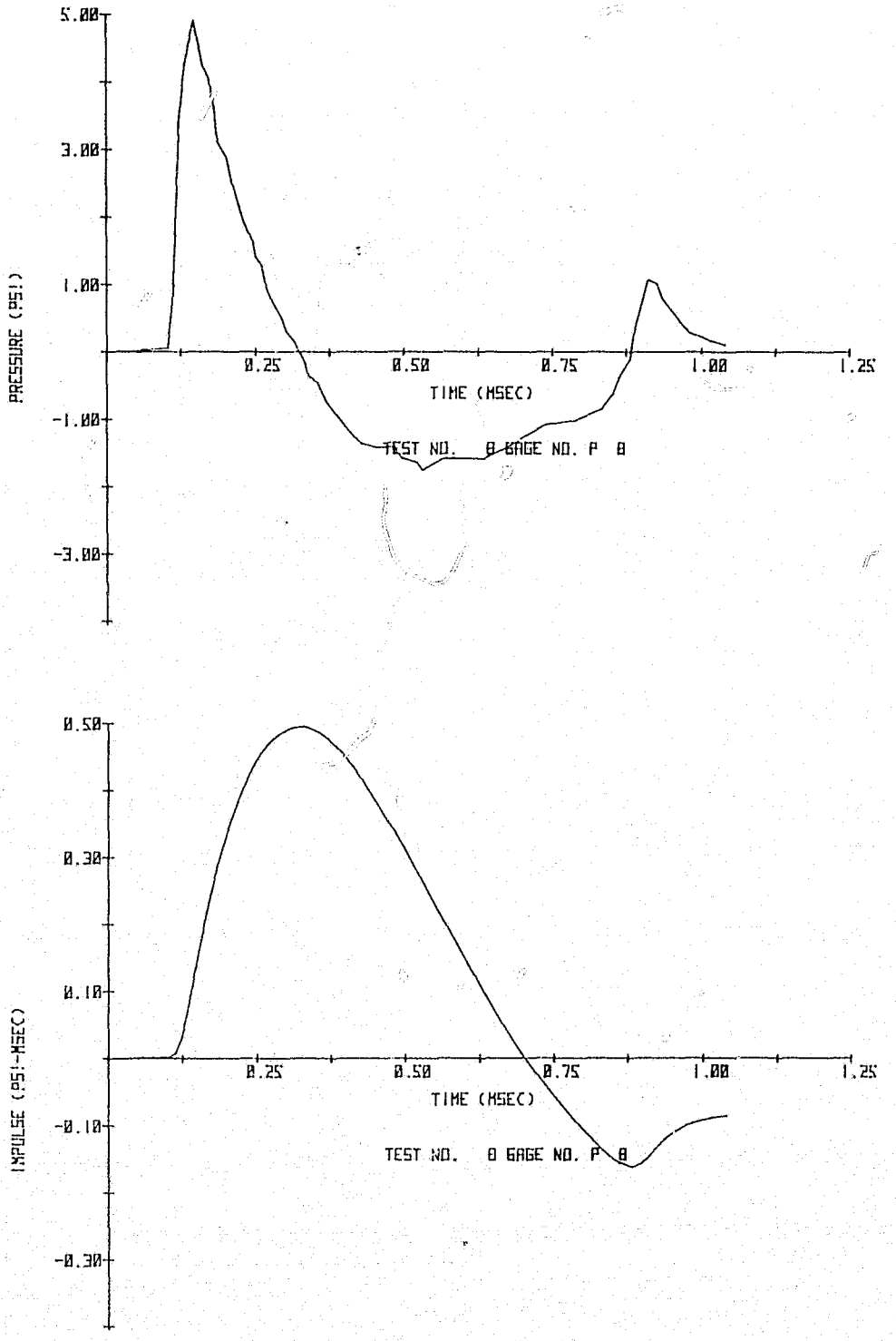

1 psi = 6.895 kPa

FIGURE 7. PRESSURE AND IMPULSE MEASURED AT $\overline{R}$ = 0.82 FROM 51 mm SPHERE PRESSURIZED WITH AIR TO 52.5 ATMOSPHERES

IV. RESULTS AND DISCUSSION

A. General

The results of this experimental effort are presented in graphical form in this section. All parameters plotted are nondimensional as derived in the model analysis in Appendix A and presented as a scaling law in Section II. Whenever possible, comparisons are made between the experimental data, and the results of theoretical calculations on non-ideal explosions and compiled data for the high explosive Pentolite.

In this program the sphere energy given in Appendix A by Equation (3) was used. However, because the glass fragments are accelerated outward as a result of the burst, their kinetic energy represents a decrease in the energy available to drive the blast wave. Therefore, fragment velocities were measured whenever possible to compute the kinetic energy of the fragments for each test. Then, a correction was made to the energy (and consequently the internal pressure) available to the blast, in a manner similar to that described by Boyer, et al [5], by subtracting the kinetic energy of the glass fragments from the total energy of the pressurized gas volume. In Figure 8, two examples of time sequences from high-speed movies show the glass spheres bursting. Note that in general the spheres "grow" relatively uniformly except for the area around the neck and the bottom portion where the pneumatic striker hits the spheres. The fragment velocity was obtained by measuring the velocities of the glass fragments along six different radials. Two of these radials were along the horizontal axis of the sphere, the other four were 45° above and below this axis on both sides. Bottom and top radials were not used because of the local effects caused by the striker and the neck of the glass sphere. These six velocities were then averaged to obtain the velocity used to compute the kinetic energy of the fragments. For those experiments in which movies were not obtained, the fragment velocity was estimated in most cases from repeat experiments in which the fragment velocity had been measured and the test setup was almost the same.

B. Nondimensional Data

The pressure-time histories that were observed from these bursting spheres were initially qualitatively similar to those from ideal explosions in that they contained a first shock which had a measurable time-of-arrival, maximum overpressure, and positive impulse. However, the latter part of the records differed from the usual point source records in that they contained a large negative phase impulse closely followed by a strong second shock. This is illustrated in Figure 5. These blast wave parameters are presented in Figures 9 through 19 in nondimensional form as functions of the corrected pressure in the sphere and the scaled distance as dictated by the reduced form of the scaling

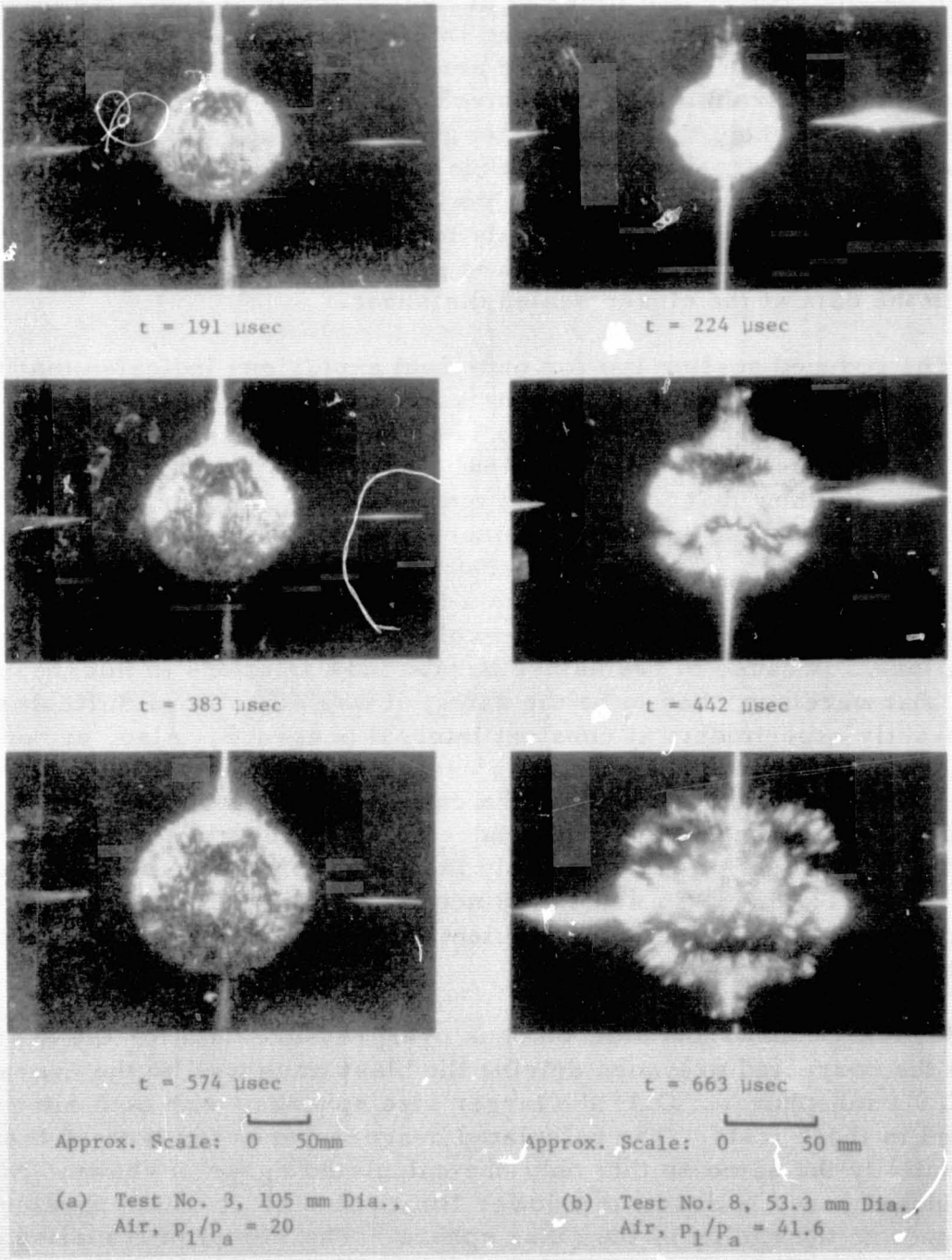

FIGURE 8. HIGH-SPEED CINEMATOGRAPHY OF BURSTING PRESSURIZED SPHERES

law in Section II. In these figures two symbols, (circles and squares), are used. The squares indicate data from tests for which fragment velocities had to be estimated. The scaled times of arrival of the first shock from the pressurized bursting spheres are presented in Figure 9 and are compared to those of Pentolite [7]. Note that the scaled arrival time t_a, of the first shock is comparable to that from a high-explosive for scaled distances $\bar{R}$ from 0.5 to 6.0. Also, note that all the data groups together within its scatter, regardless of the internal pressure in the sphere for corrected sphere pressure ratios of 9.9 to 42. Also, notice that the scatter in the data increases with a decreasing $\bar{R}$. This is due primarily to the fact that as events occur at shorter times, poorer time resolution is possible, and thus more scatter occurs in the data at the closer scaled distances.

The reduced scaling law for non-ideal explosions indicates that the peak overpressure, in addition to being a function of the scaled distance $\bar{R}$ and the pressure in the sphere p_1/p_a, is also a function of the specific heat ratio γ_1 of the gas in the sphere. Analytical computations of non-ideal blast waves [8] show that for constant temperatures the overpressure depends primarily on $\bar{R}$, but as the pressure increases the overpressure becomes a weak function of p_1/p_a and γ_1. Therefore, the experimental overpressure data are presented in Figures 10-13 as a function of $\bar{R}$, p_1/p_a and γ_1, and compared to data from Pentolite high-explosive compiled data and analytical computations. Because of premature bursts and variations in thickness in spheres that were supposed to be the same, it was sometimes difficult to repeat exactly experiments at constant internal pressure. Also, because it is difficult to predict the scaled kinetic energy of the fragments before the tests so that similar experiments of the same net internal pressure using two different size spheres could be conducted, the overpressure data have been grouped into sets of approximately the same corrected internal pressure ratios of about 12, 18.5, 26 and 42. Since the temperature θ_1 of the gas in the sphere was the same as the ambient temperature θ_a the temperature ratio for all the tests was one.

Figure 10 shows the side-on peak overpressure data for the experiments in which the corrected pressure driving the blast wave was on the average about 12.0 atmospheres. Only the larger size spheres, with both air and argon, were used in these tests. The calculated overpressures for both of these gases are essentially the same so that only one calculated curve is shown. Note that the calculated curve is drawn to a lower limit value of $\bar{R}$ which physically corresponds to the radius of the glass sphere. The Pentolite compiled data are also shown for comparison. Figure 11 shows a similar data comparison for tests with corrected pressures in the sphere of about 18.5 atmospheres. All the experimental data in this set of tests, except for one point, are from tests using the smaller spheres with both air and argon. Figure 12 is a graph of the data for the tests using internal pressures of about 26 atmospheres.

Data points from both size spheres and gases are included in this group. Finally, Figure 13 shows the data from a small sphere test using air at a pressure of 42 atmospheres. Notice that in all four of these figures the measured overpressures are lower than those calculated, and that both of these are always lower than for Pentolite high-explosive. The lower experimental pressures are due to the finite bursting time of the glass spheres. This would be expected because the main shock wave is not formed immediately [5] and must be formed from the gas flow around the glass fragments. Thus, the maximum calculated contact surface pressure ratio will never be realized when a frangible wall is present.

The scaled duration data of the first positive overpressure are shown in Figure 14 and compared to the Pentolite curve. As was the case with the arrival time data, the scaled duration does not appear to be dependent on the internal pressure of the gas in the sphere, at least within the scatter of the data. However, the data does seem to group together depending on the type of gas, with the data from the argon experiments yielding longer scaled times than the air tests thus showing a weak function on the specific heat ratio which characterizes the gas in the sphere. Both sets of durations, though, are longer than the Pentolite scaled durations at the tested scaled distances of 0.5 to 6.0.

The scaled impulse data from the first positive phase of the pressure-time trace are shown in Figure 15 and compared to the Pentolite compiled data. The impulse also does not seem to depend on the pressure of the sphere at pressure ratios ranging from 9.9 to 42. As would be expected from the scaled duration data, the impulse from the argon tests groups together and is consistently higher than the air data. The Pentolite curve seems to fall between the two groups of data.

As previously mentioned, the character of the blast wave data from a bursting sphere is such that a large negative phase, as compared to Pentolite or other high-explosives, occurs. Figure 16 is a graph of the scaled duration of this negative phase. As was the case for the positive phase duration, the negative phase duration groups into two distinct sets, one for air and one for argon. Since no quantitative data exists for this parameter from Pentolite, no comparison is made in this figure. Again the scaled duration data does not seem to be dependent on the pressure within the sphere.

The negative phase impulse data are shown in Figure 17 for all the tests in this program. These data scatter slightly more than the positive phase impulse but again they group more or less into two sets with the argon data being slightly higher than the air data. Within the scatter of the data, this impulse data seems independent of the pressure in the sphere. By comparing

these two sets of data with the positive phase impulse of Figure 15, one can see that the negative phase impulse values are slightly higher at corresponding scaled distance. This is very different than results from the more ideal explosions caused by Pentolite or similar high-explosives in which the negative phase impulse is relatively much smaller than the positive phase impulse.

The scaled arrival times of the second shock are plotted in Figure 18. As was the case for the arrival time data for the first shock, these data appear to be independent of the internal gas pressure in the sphere. On the other hand, the scaled time of arrival data of the second shock seems to group together depending on the gas in the sphere.

Finally, Figure 19 shows the peak overpressure data of the second shock front for bursting gas spheres. These data scatter much more than the first shock overpressure and therefore the weak dependence of overpressure on the internal pressure of the sphere cannot be discerned, if it exists for the second shock. Consequently, all the data are plotted together. Comparing first and second shock peak overpressures at same values of $\bar{R}$, one can see that the second peak pressures are of significant amplitude.

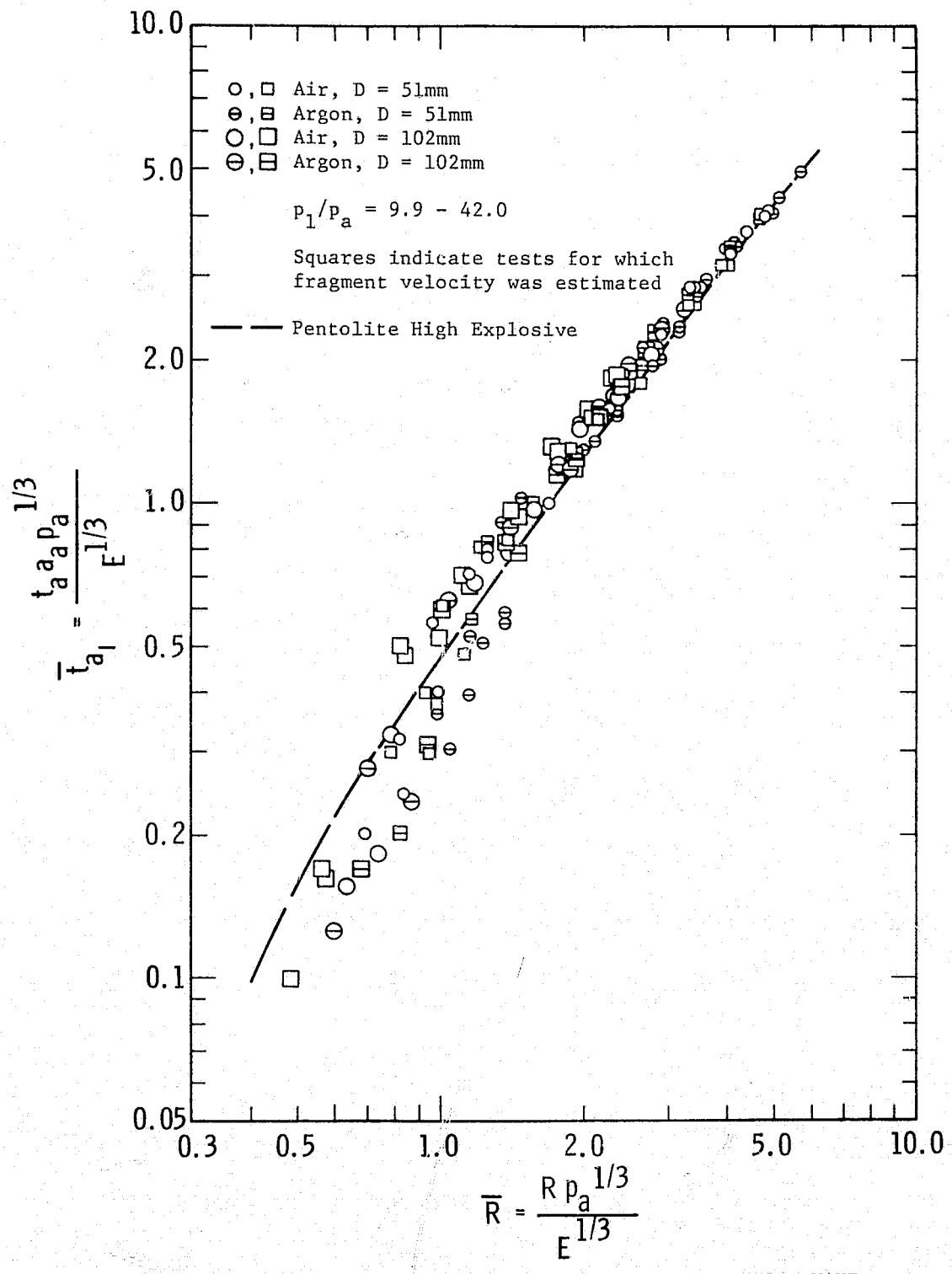

FIGURE 9. SCALED TIME OF ARRIVAL OF FIRST SHOCK WAVE FROM BURSTING GAS SPHERE

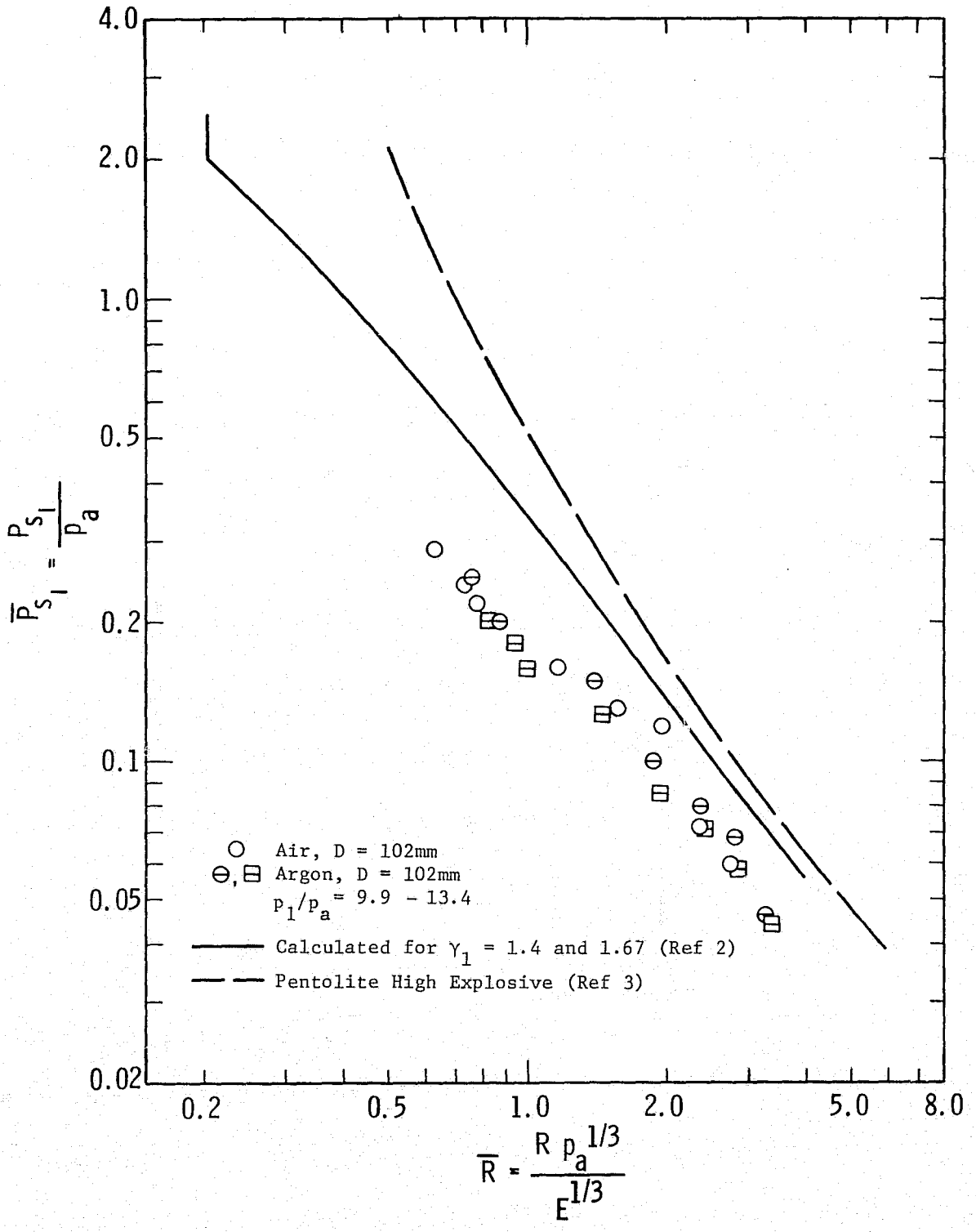

FIGURE 10. SCALED SIDE-ON PEAK OVERPRESSURE FOR BURSTING GAS SPHERE WITH p_1/p_a = 12.0, T_1/T_a = 1.0

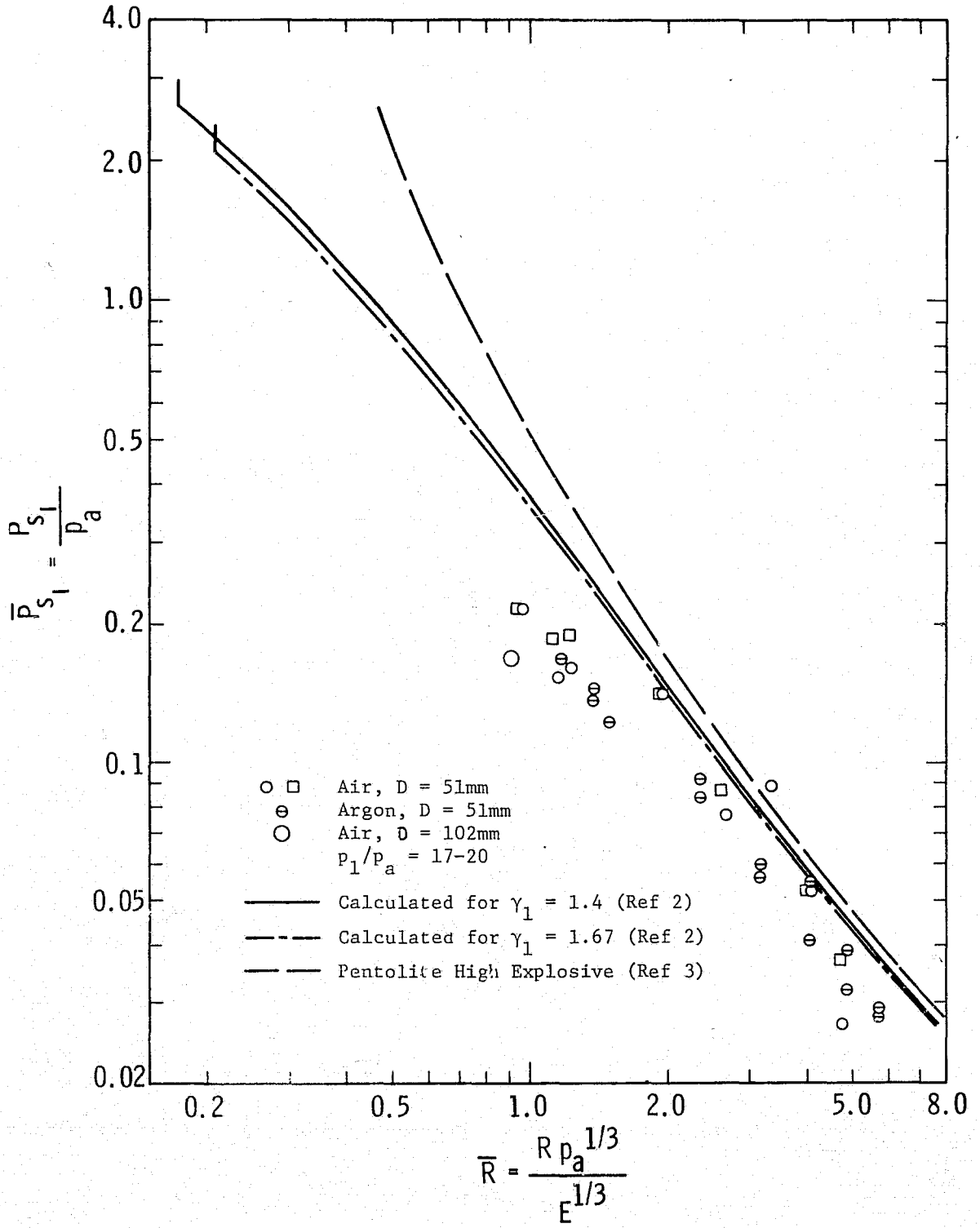

FIGURE 11. SCALED SIDE-ON PEAK OVERPRESSURE FOR BURSTING GAS SPHERE WITH p_1/p_a = 18.5, T_1/T_a = 1.0

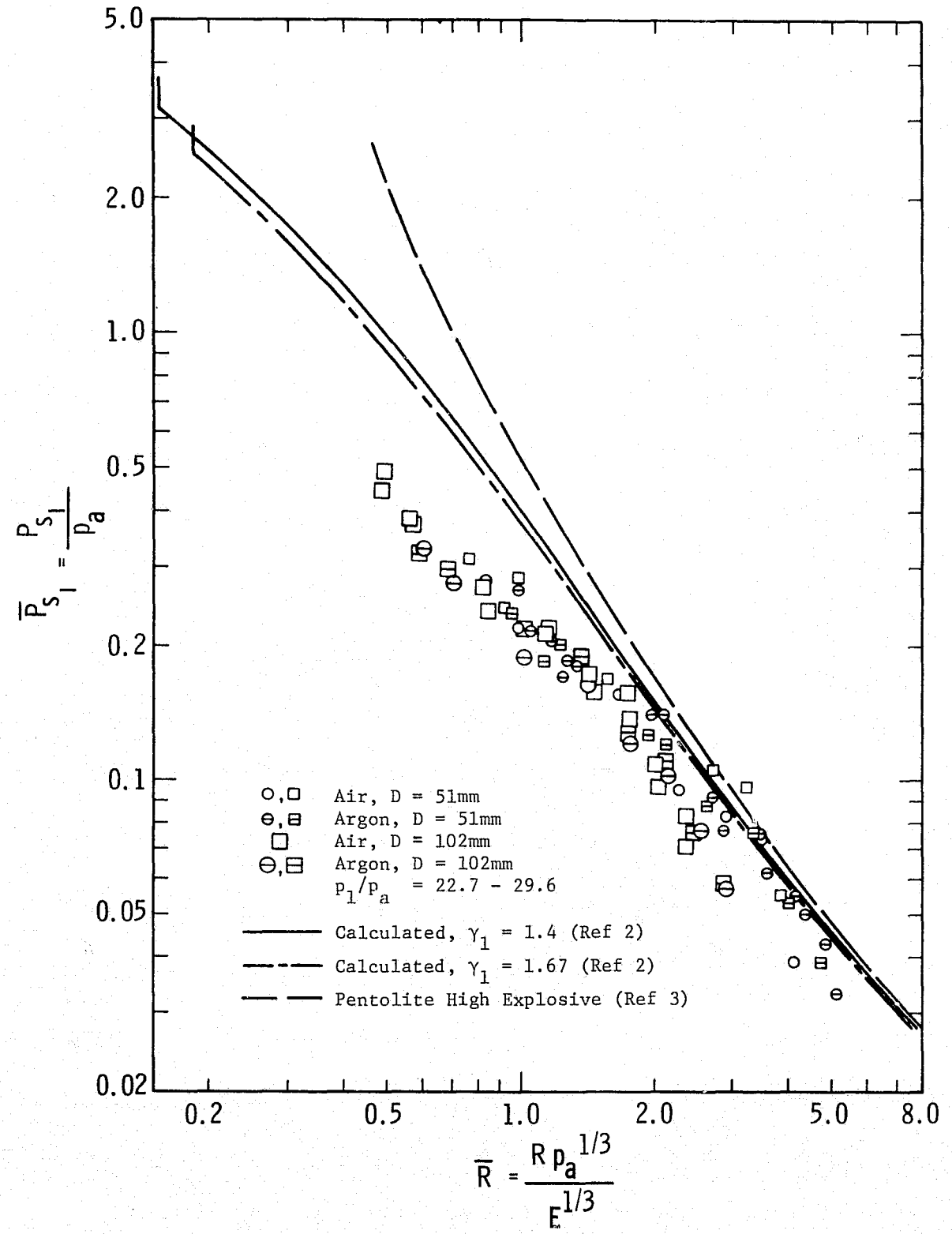

FIGURE 12. SCALED SIDE-ON PEAK OVERPRESSURE FOR BURSTING GAS SPHERE WITH p_1/p_a = 26, T_1/T_a = 1.0

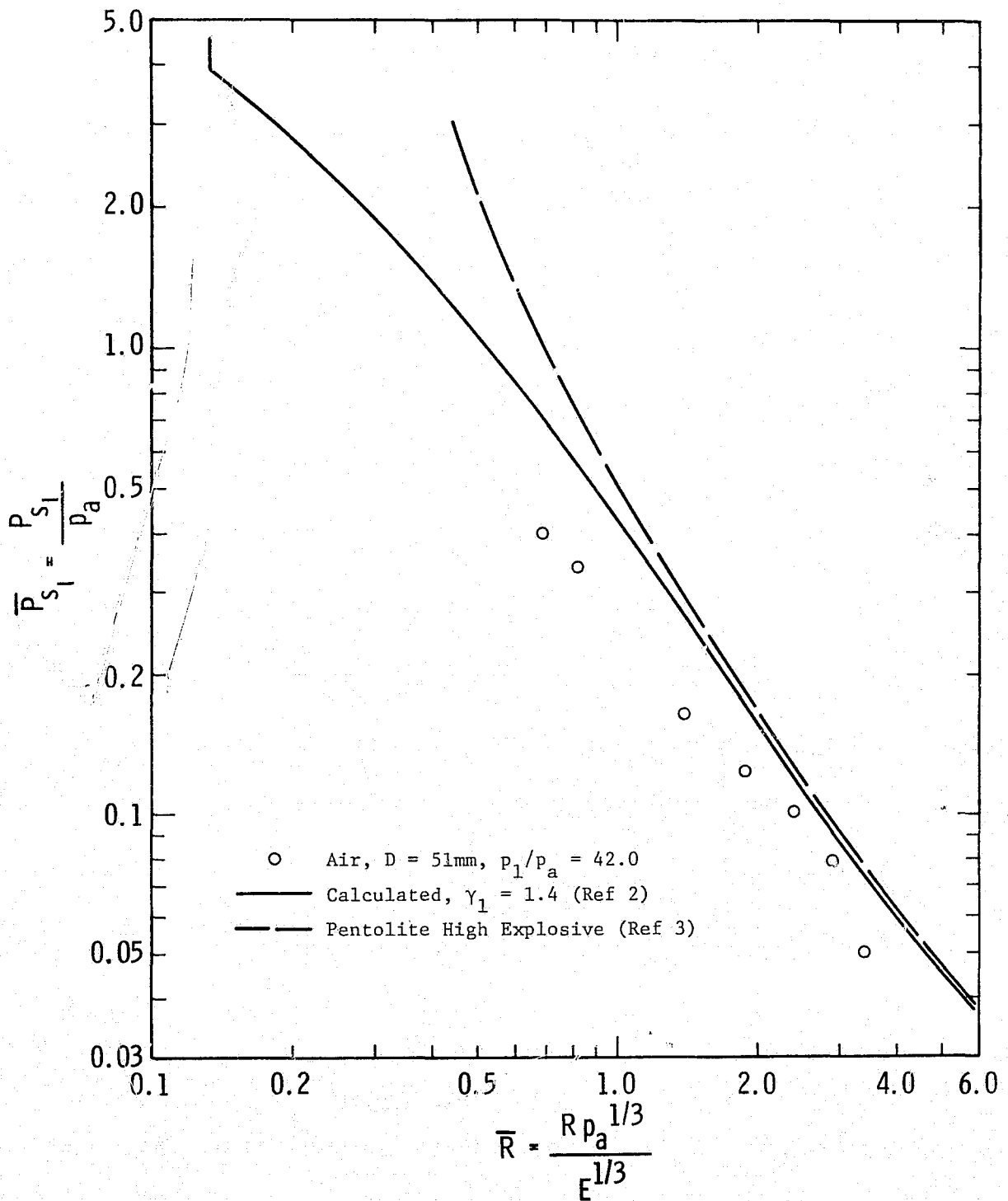

FIGURE 13. SCALED SIDE-ON PEAK OVERPRESSURE FOR BURSTING GAS SPHERE WITH p_1/p_a = 42.0, T_1/T_a = 1.0

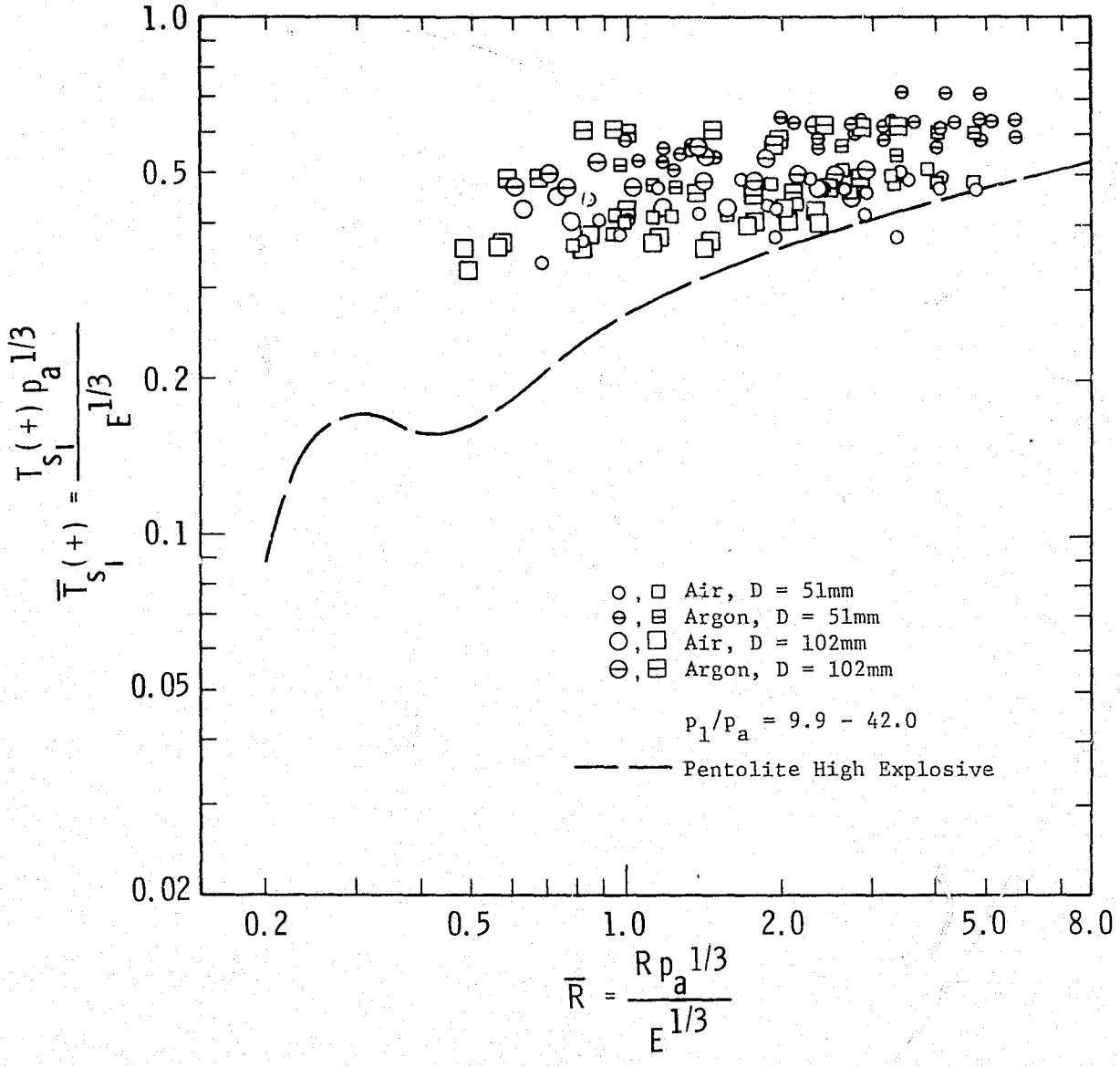

FIGURE 14. SCALED DURATION OF FIRST POSITIVE PHASE OF BLAST WAVE FROM BURSTING GAS SPHERES

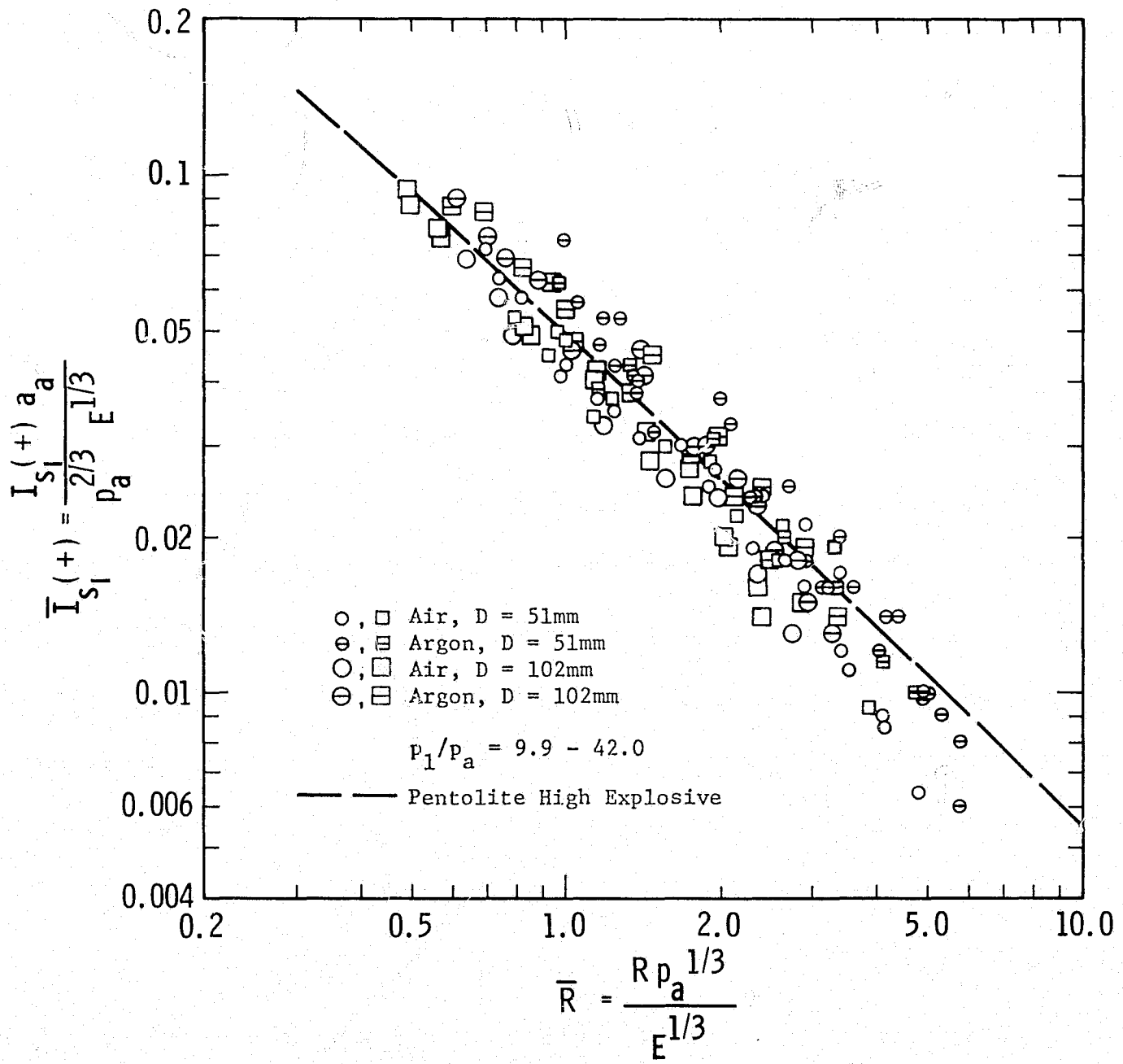

FIGURE 15. SCALED SIDE-ON POSITIVE IMPULSE FROM BURSTING GAS SPHERE

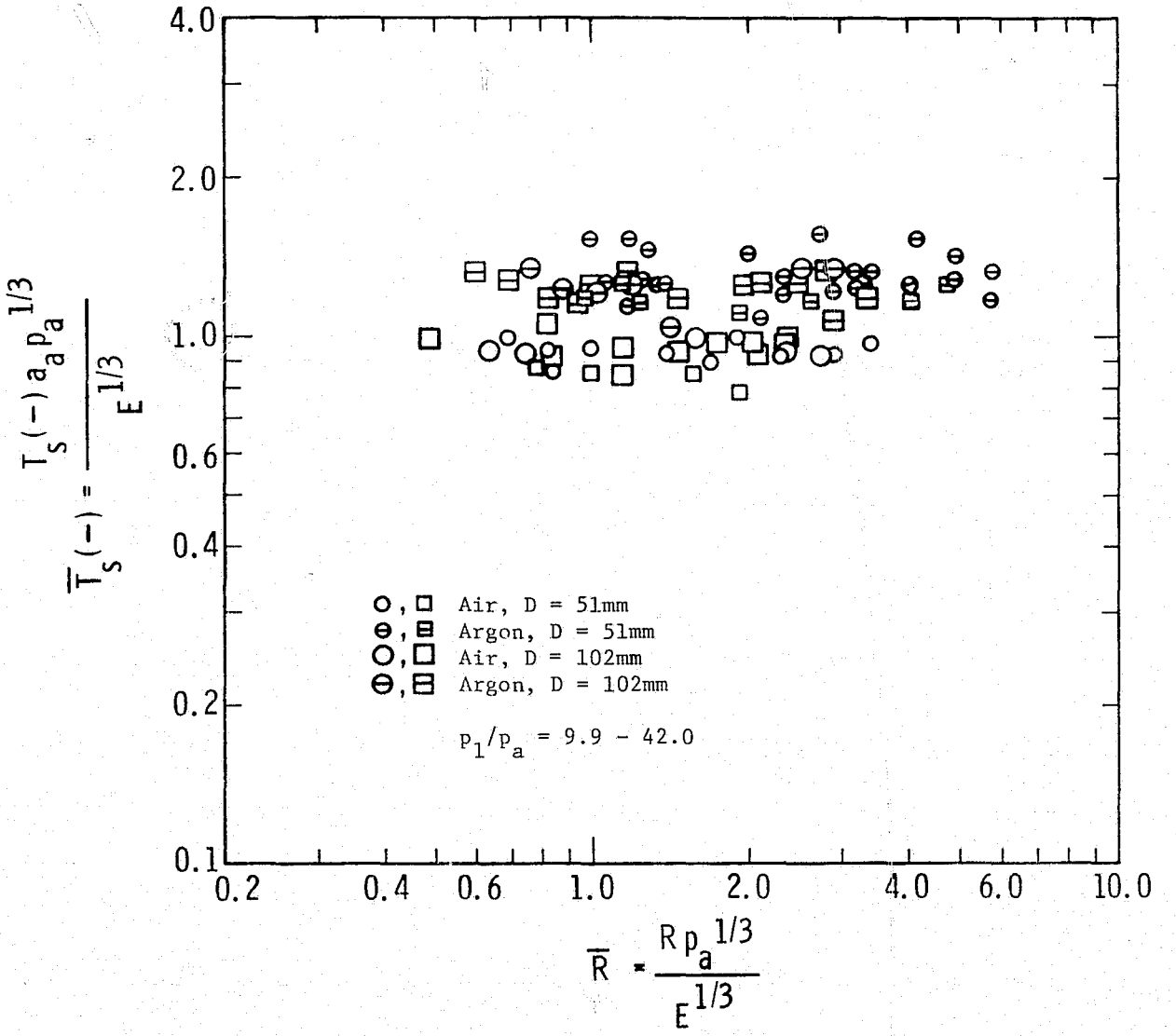

FIGURE 16. SCALED DURATION OF NEGATIVE PHASE OF BLAST WAVE FROM BURSTING GAS SPHERE

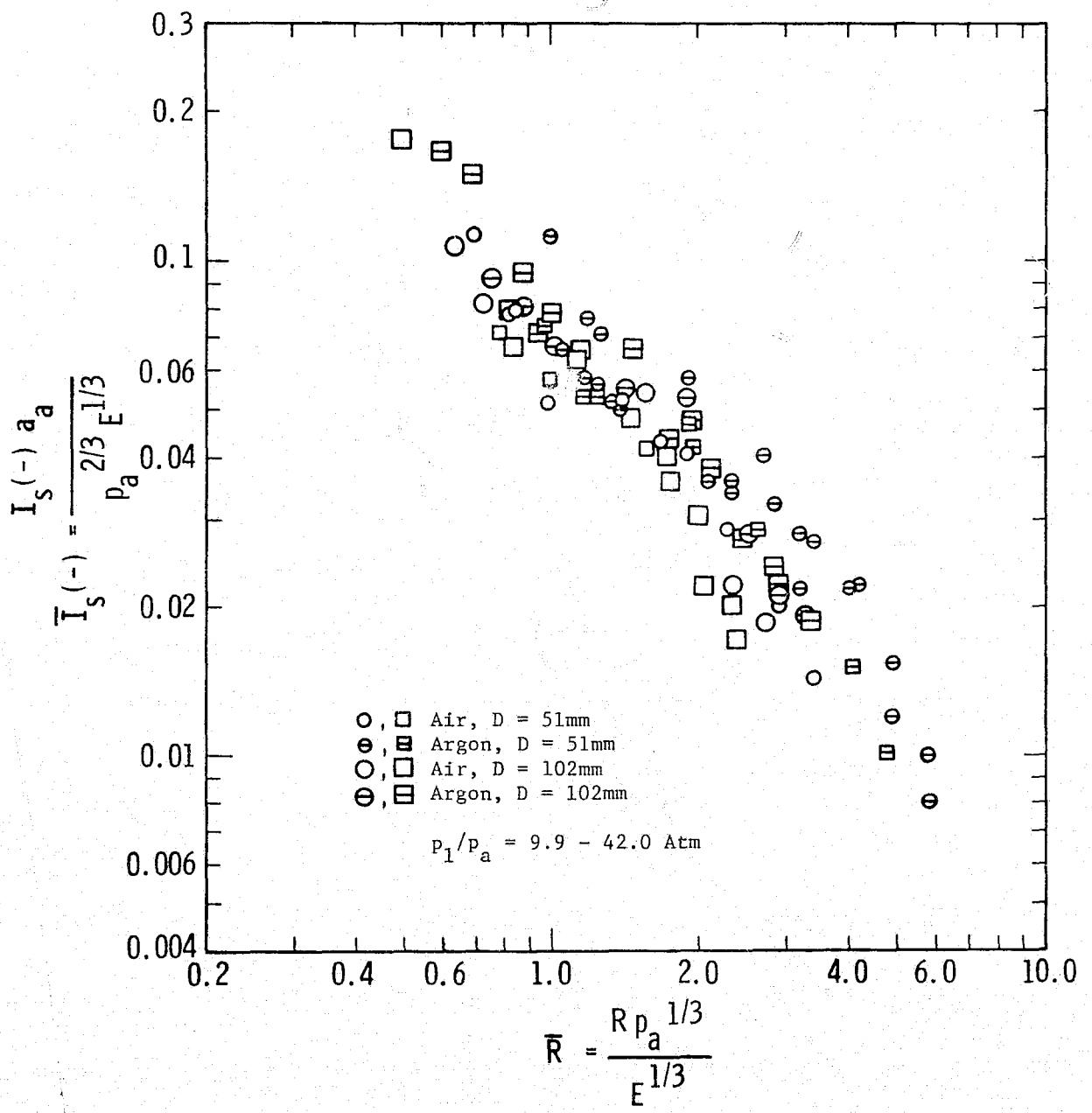

FIGURE 17. SCALED SIDE-ON NEGATIVE IMPULSE FROM BURSTING GAS SPHERE

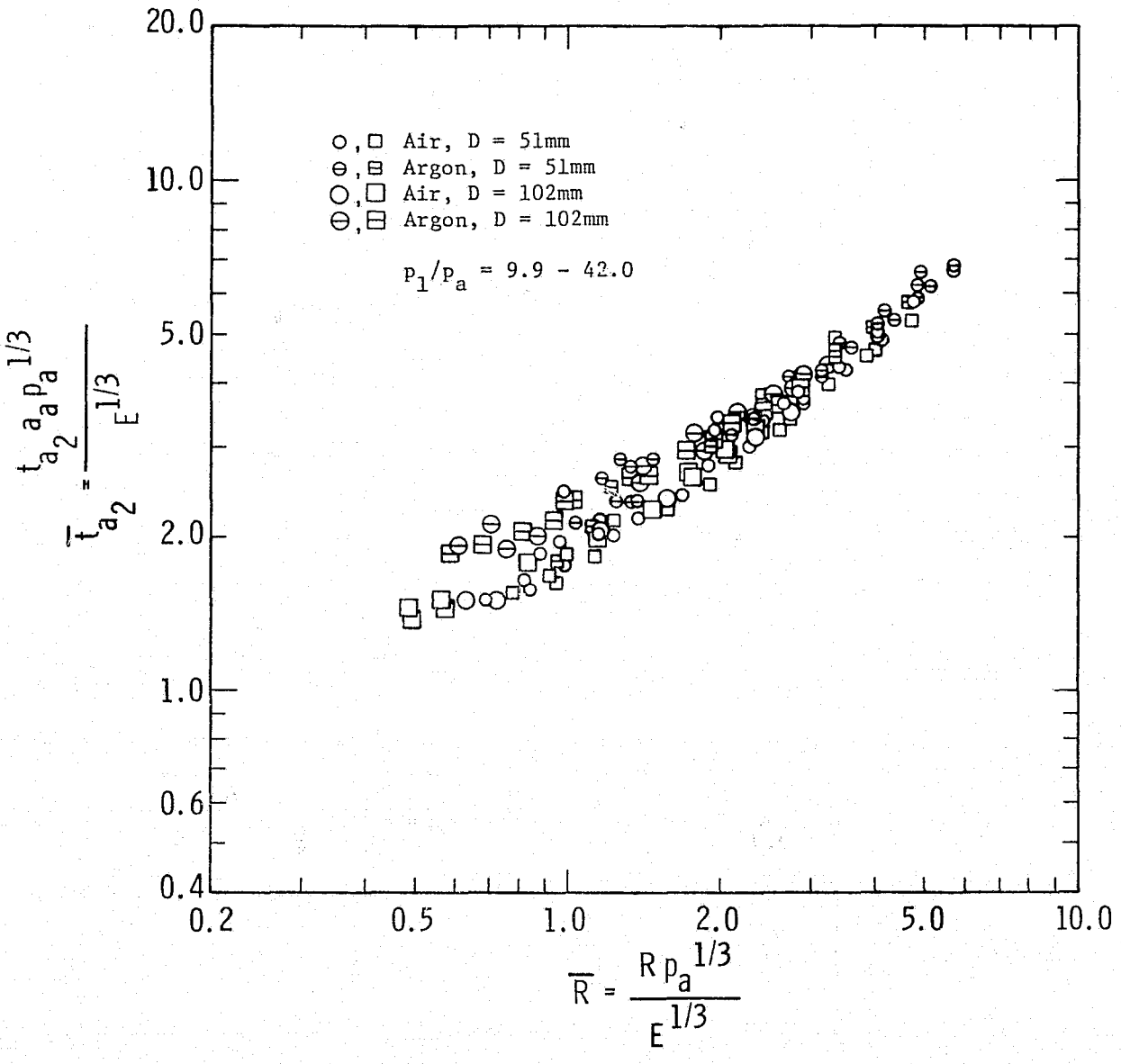

FIGURE 18. SCALED TIME OF ARRIVAL OF SECOND SHOCK WAVE FROM BURSTING GAS SPHERE

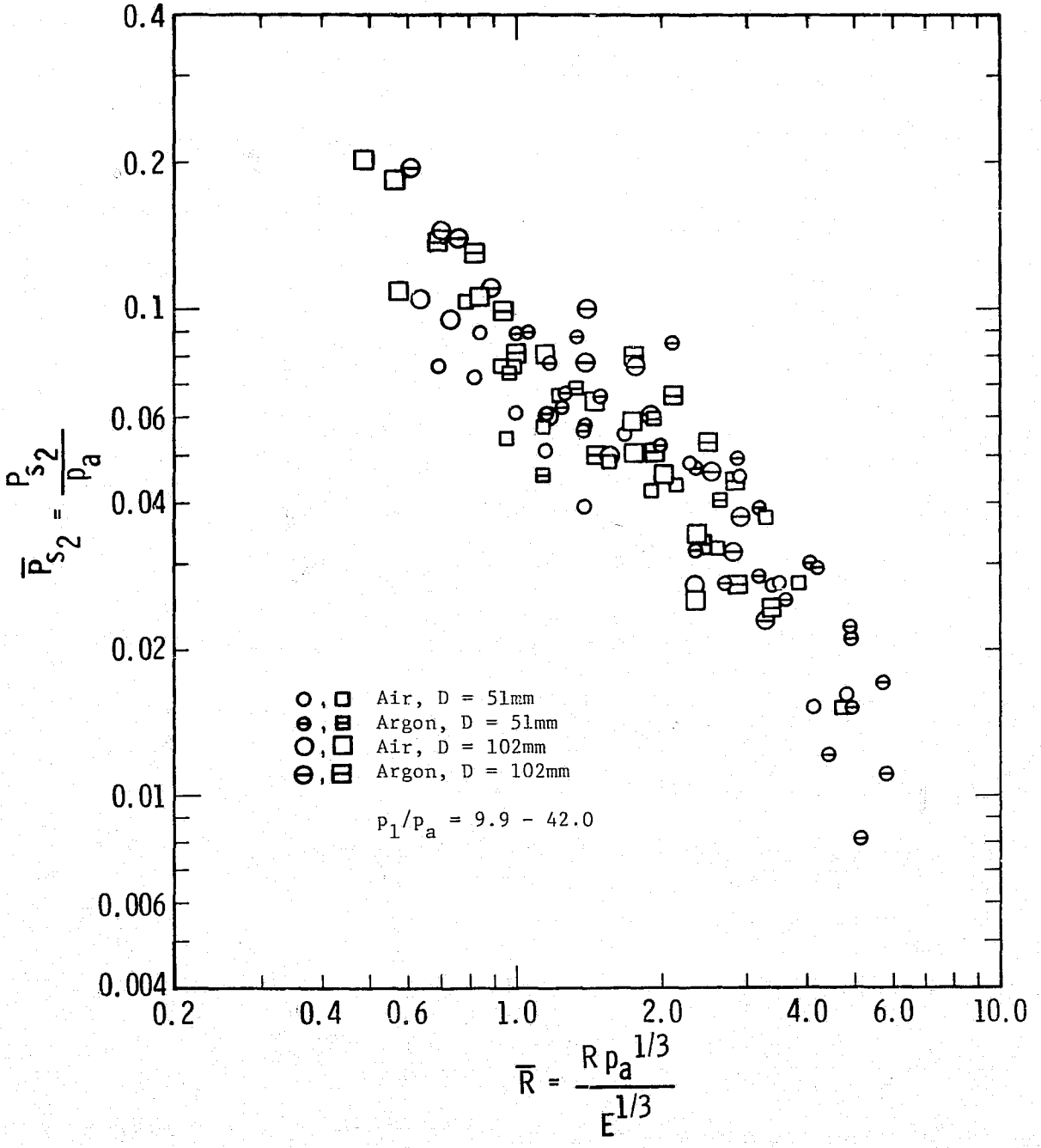

FIGURE 19. SCALED SIDE-ON PEAK OVERPRESSURE OF SECOND SHOCK FOR BURSTING GAS SPHERE

V. CONCLUSIONS

Because of the lack of detailed measurements of the blast waves from non-ideal explosions, Southwest Research Institute conducted small-scale experiments to obtain data on incident overpressure at various distances from bursting, pressurized spheres. Glass spheres of two different sizes and various thicknesses were pressurized and shattered by a pneumatic striker to create the non-ideal blast waves. Two different gases, air and argon, were used in the 51 and 102 mm (2 and 4 in) diameter spheres to pressures ranging from 12.2 to 53.5 atmospheres.

Complete time histories of overpressure were obtained by an array of eight side-on pressure transducers located at different stand-off distances, some as close as was physically possible. Data were obtained from all eight channels of instrumentation on almost every test. High-speed cinematography was used in the majority of the tests to observe sphere break up and obtain velocities of the glass fragments. The velocities were used to compute the kinetic energy of the fragments for correcting the energy in the sphere due to the high-pressure gas for driving the blast waves.

The characteristics of the recorded blast waves proved to be quite repeatable, and somewhat different from waves from condensed explosives such as Pentolite or TNT. The initial positive phase is followed by a very pronounced negative phase and a much more distinct second shock occurs. Reduced data from these experiments include the peak overpressures for both first and second shocks, times of their arrival, durations of first positive phase and negative phase, and the positive and negative phase impulses. The data were scaled in accordance with a scaling law presented in this report, and compared whenever possible with results of theoretical calculations and compiled data for Pentolite high-explosive. The waves are qualitatively similar to waves from Pentolite in some respects but distinctly different in other respects. First shock arrival times and positive impulse are similar. Basic differences are lower initial overpressure, longer positive phase duration, much larger negative phase (which in general is larger than the positive phase impulse), and a strong second shock. As compared to the theoretical calculations, the measured initial overpressures are lower.

All the scaled data obtained in this program depend primarily on the scaled distance as defined by the model law used. However, scaled times of arrival, durations, and impulses appear to also be weak functions of the type of gas in the sphere. The model law for non-ideal explosions characterizes the gas in the sphere by the specific heat ratio. This law also predicts that the scaled blast parameters are a function of the initial pressure in the sphere. However, except for the scaled overpressure of the first shock, no dependence on the initial pressure can be established within the scatter of the data.

The data presented appear to be the first sizeable set of measurements of the characteristics of blast waves from bursting, frangible pressure spheres. The differences cited between blast waves from bursting spheres and high explosives show that those from pressurized spheres are indeed non-ideal, even though they are quite repeatable. Close to these sources the concept of "TNT equivalence" appears to have little meaning because the blast waves differ too greatly from those from TNT. Because of the lower initial over-pressure, but larger negative phase and strong second shock the damage caused by these waves can be significantly different, too, depending on the particular "target" placed in its path.

VI. RECOMMENDATIONS

The experiments reported here indicate significant differences in the characteristics of the blast waves generated when frangible gas pressure spheres burst and the blast waves from condensed explosive sources. But, the test data are limited to two gases, air and argon, with properties which do not differ greatly. To supplement these data, we recommend additional experiments using the basic test arrangement and methods reported here. These experiments should probably include:

(1) Tests of bursting spheres completely filled with liquids of high vapor pressure. The liquids could be freons, CO_2, or sulfur hexafluoride (SF_6).

(2) More tests of inert gas-filled spheres, using helium (which has $\gamma = 5/3$, as does argon, but a much higher sound velocity), and perhaps a gas with a low γ, such as a freon or SF_6 in the gaseous state.

(3) Combustion experiments, using thin glass spheres as envelopes to contain combustible gaseous mixtures. The mixtures could be propane-air, acetylene-air, acetylene-oxygen, or hydrogen-oxygen.

Because the data reported here show significant negative phase pressures and impulses as well as strong second shocks, we also recommend that computations of non-ideal blast wave properties, such as those reported in References 4 and 8, be carried out for longer scaled times for comparison with the measurements. These differences in blast wave properties from TNT or point source explosions can significantly alter the blast loading from that previously used, because most of the past work has ignored both the negative phase of the blast wave and any shocks after the first. This in turn can seriously alter damage predictions based on "TNT equivalence". If the blast wave properties reported here turn out to be typical of the various classes of non-ideal explosions to be tested and/or analyzed we would also recommend a review and revision of present prediction methods in Reference 8 for loading of structures by non-ideal explosions. A last recommendation is that present analyses be modified to account for the mechanisms of fragment breakup and acceleration in a more exact manner than the simple energy balance we have used.

APPENDIX A

MODEL ANALYSIS

To aid in casting results of analyses or experiments in the most general form, a model analysis is desirable. This particular analysis is limited to blast waves generated by pressure spheres burst in "free air", i.e., away from the ground surface. The effects on the blast wave of the pressure container or the fragments from this container are not considered. The blast source is therefore idealized as a sphere of gas at an initial pressure higher than atmospheric which is suddenly released from a massless spherical shell at time zero. We wish to establish scaling laws for the subsequent formation and transmission of blast waves through the atmosphere.

The first step in developing a scaling law is to list all pertinent physical parameters, together with their fundamental dimensions, in a force, length, time, temperature (F, L, T, θ) system. This is done in Table 1. As will be seen later, some parameters are superfluous, but are retained for now and discarded later. The twenty-two parameters are grouped so that some describe the blast source, some describe ambient air conditions, and others describe the characteristics of the blast wave.

The dimensional parameters are next combined into a lesser number of dimensionless groups (often called pi terms) by the methods of dimensional analysis. The intermediate steps are merely algebraic and will not be given here. The number of dimensionless groups equals the number of original dimensional parameters minus the number of fundamental dimensions, i.e., 22 - 4 = 18. The actual grouping is not unique; one possible set is given in Table 2 with some physical description or interpretation for each term or set of terms. Table 2 can be considered as a model law which requires identification of <u>all</u> terms in the table if tests or analytical results on different scales are to be compared.

The number of terms can be reduced by applying some physical restrictions. Restricting ourselves to perfect gas behavior throughout the system, the following equations apply

$$a_1^2 = \gamma_1 \frac{p_1}{\rho_1} = \gamma_1 \frac{R^*}{M_1} \theta_1 \qquad (1)$$

$$a_a^2 = \gamma_a \frac{p_a}{\rho_a} = \gamma_a \frac{R^*}{M_a} \theta_a \qquad (2)$$

where R^* is the universal gas constant and M_i is molecular weight of the i^{th} gas. Then, from Equation (2), terms π_7 and π_8 are exactly equivalent and one of them is therefore superfluous. We can also drop π_8 by itself because this parameter never changes (we are always transmitting our blast waves through air). In a similar way, Equation (1) can be used to eliminate one of the terms

TABLE 1. LIST OF PARAMETERS

Parameter	Symbol	Dimensions
Source		
Energy	E	FL
Radius	r_1	L
Temperature	θ_1	θ
Pressure	p_1	FL^{-2}
Ratio of specific heats	γ_1	--
Density	ρ_1	FT^2L^{-4}
Sound velocity	a_1	LT^{-1}
Air		
Pressure	p_a	FL^{-2}
Density	ρ_a	FT^2L^{-4}
Temperature	θ_a	θ
Ratio of specific heats	γ_a	--
Sound velocity	a_a	LT^{-1}
Blast wave		
Overpressures (side-on and reflected)	P_s, P_r	FL^{-2}
Density	ρ	FT^2L^{-4}
Temperature	θ	θ
Shock velocity	U	LT^{-1}
Particle velocity	u	LT^{-1}
Arrival time	t_a	T
Duration	T	T
Impulse	I	FTL^{-2}
Radius	R	L

TABLE 2. DIMENSIONLESS (PI) TERMS

No.	Term	Description
π_1	$(E/r_1^3 p_a)$	Scaled energy
π_2	(θ_1/θ_a)	Scaled source properties
π_3	(p_1/p_a)	
π_4	γ_1	
π_5	(ρ_1/ρ_a)	
π_6	(a_1/a_a)	
π_7	$(\rho_a a_a^2/p_a)$	Scaled ambient conditions
π_8	γ_a	
π_9	(P_s/p_a)	Scaled blast wave properties
π_{10}	(P_r/p_a)	
π_{11}	(ρ/ρ_a)	
π_{12}	(θ/θ_a)	
π_{13}	(U/a_a)	
π_{14}	(u/a_a)	
π_{15}	$(t_a a_a p_a^{1/3}/E^{1/3})$	
π_{16}	$(T a_a p_a^{1/3}/E^{1/3})$	
π_{17}	$(I a_a p_a^{1/3}/E^{1/3})$	
π_{18}	$(R\, p_a^{1/3}/E^{1/3})$	Scaled distance

π_3 through π_6, after some combination. Equations (1) and (2) also allow us to calculate the temperature ratio π_2, once other state parameters are known. If we wish, we can eliminate a number of the scaled blast wave parameters by invoking the Rankine-Hugoniot equations (see Reference 7, Chapters 2 and 6). Since π_8 is fixed and π_9 is known, all of the other blast front parameters π_9 through π_{13} can be uniquely determined by use of these equations. However, we will ratain them to show the dimensionless forms of the blast wave properties.

If we accept Huang and Chou's definition of energy [3] it is, in the notation used here,

$$E = \frac{4\pi}{3} \frac{(p_1 - p_a)}{(\gamma_1 - 1)} r_1^3 \tag{3}$$

Substituting in π_1, we get

$$\pi_1 = \left[\frac{4\pi}{3p_a} \frac{(p_1 - p_a)}{(\gamma_1 - 1)} \right] \tag{4}$$

We can see that π_1 is a unique function of π_3 and π_4, so we can eliminate one of these three terms with no loss of generality. Because π_1 is more complex in form than the others, we eliminate it.

Using the restrictions noted above, we will write the scaling law in a condensed and somewhat different form as follows:

$$\left.\begin{array}{l} (P_s/p_a) \\ (P_r/p_a) \\ (\rho/\rho_a) \\ (\theta/\theta_a) \\ (U/a_a) \\ (u/a_a) \\ (t_a a_a p_a^{1/3}/E^{1/3}) \\ (Ta_a p_a^{1/3}/E^{1/3}) \\ (Ia_a p_a^{2/3}/E^{1/3}) \end{array}\right\} = f_i \left[(p_1/p_a),\ \gamma_1,\ (a_1/a_a),\ (Rp_a^{1/3}/E^{1/3}) \right] \tag{5}$$

The symbolism f_i indicates that each of the scaled blast wave properties on the left side of Equation (5) is a different function of the five scaled parameters on the right hand side. The first three quantities on the right hand side are all scaled source properties while the last is scaled distance. (If the first three parameters do not change, the law reduces to Sachs' law [see Reference 7, Chapter 3]).

The scaling law does not and cannot tell us what the functional forms f_i are, nor does it tell us the relative importance of varying each of the parameters in the bracket in Equation (5). We must rely on either analysis or experiment or both to get these answers. What it does do is to show a convenient way of presenting results of tests or analyses, or comparing results from various investigators. Ideally, one should vary each of the first three parameters in the bracket in Equation (5) while holding the others constant, and determine the scaled blast parameters as functions of scaled distance. Huang and Chou [3] have already done this in their calculations for two parameters, because their π_o is exactly our π_3, and their η is our π_5. They did not show or vary π_4 (or equivalently, π_2). Basically, the graphical presentations such as Figure 16 in Huang and Chou [3] are a good way of presenting results of calculations, because they are totally in the form of dimensionless groups (Note that the abscissa of this figure is in error by $10^{1/3}$). We feel that π_6 is a better group to vary than π_5, but one cannot quibble with their choice if all possible groups are varied.

In the experiments reported here, we measured side-on overpressure arrival times and durations, and side-on positive and negative impulses. We did not observe reflected parameters, nor temperatures, densities or velocities. So, we can strike the corresponding scaled quantities from the left hand side of Equation (5). This involves little loss of generality because the shock-front properties and reflected overpressure are easily calculated from the measured quantities, as noted before. Also in these tests, only air and argon were used as pressurized gases in the blast wave source. For air $\gamma_1 = 1.4$ and for argon $\gamma_1 = 1.667$, which is a minor difference. The pi term a_1/a_a equals one for air and very nearly one for argon. We therefore used a reduced form of the scaling law with barred quantities indicating nondimensional quantities corresponding to the desired dimensional quantity. This form is:

$$\left.\begin{aligned} \bar{P}_s &= \left(\frac{P_s}{p_a}\right) \\ \bar{t}_a &= \left(\frac{t_a a_a p_a^{1/3}}{E^{1/3}}\right) \\ \bar{T} &= \left(\frac{T a_a p_a^{1/3}}{E^{1/3}}\right) \\ \bar{I}_s &= \left(\frac{I_s a_a}{p_a^{2/3} E^{1/3}}\right) \end{aligned}\right\} = f_i\left[\left(\frac{p_1}{p_a}\right), \frac{R p_a^{1/3}}{E^{1/3}}\right] \qquad (6)$$

where

p_a = ambient pressure (absolute)

a_a = ambient sound velocity

p_s = peak side-on overpressure

t_a = arrival time of the peak overpressure

T = duration of the overpressure

I_s = specific impulse

R = radius of blast wave (standoff distance)

p_1 = internal absolute pressure of sphere

E = internal energy in the sphere

$$\bar{R} = \frac{R\, p_a^{1/3}}{E^{1/3}}$$

APPENDIX B

DATA TABLES

The nondimensional data plotted in all the graphs in this report are presented here in tabular form along with measured characteristics of the glass spheres used in each test. Most of the column headings are self-explanatory; however, a short explanation of each follows:

- Volume - the actual volume measured for each sphere.
- Computed Dia. - the diameter of the sphere as computed from the measured volume.
- Mass - the mass of the glass sphere obtained by taking the difference of the total mass of the sphere assembly before the test and the mass of the remains on the test fixture after the test.
- Thickness - computed from the measured mass and diameter of the sphere, and specific gravity of the glass.
- γ_1 - table value for the specific heat ratio of the gas used in the sphere.
- Fragment Velocity - the average velocity measured using high-speed cinematography. Approximate values are for tests which burst prematurely and movies were not obtained.
- Corrected Pressure Ratio - internal pressure in the sphere computed using Equation (3) and subtracting the kinetic energy of the fragments.
- All nondimensional parameters used have been defined in Equation (6). The local atmospheric constants used in some of these parameters were:

  $p_a = 98.5$ kPa $= 14.3$ psi

  $a_a = 339.3$ m/s $= 13,360$ in/sec

- Example computation of corrected Pressure Ratio (p_1/p_a) for Test No. 1.

  Kinetic Energy:

$$K.E. = \frac{m V^2}{2} = \frac{(.091 \text{ kg})(68.5 \text{ m} \cdot \text{s}^{-1})^2}{(2)(\text{J}^{-1} \cdot \text{m}^2 \cdot \text{kg} \cdot \text{s}^{-2})}$$

$$K.E. = 44.58 \text{ J}$$

Pressure Energy in Sphere:

$$E' = \frac{V(p_1' - p_a)}{\gamma_1 - 1} \quad \frac{(65.5\ cm^3)(2,068,200\ N \cdot m^{-2})(J \cdot N^{-1} \cdot m^{-1})}{(0.4)(10^6\ cm^3 \cdot m^{-3})}$$

$$E' = 338.67\ J$$

Net Energy Available for Driving Blast Wave:

$$E = E' - KE = 294.09\ J$$

Equivalent Corrected Pressure Ratio in Sphere:

$$(p_1 - p_a) = \frac{E(p_1' - p_a)}{E'} = \frac{(294.09)(2,068,200\ Pa)}{(338.67)}$$

$$(p_1 - p_a) = 1,795,900\ Pa$$

$$p_1 = 1,894.4\ kPa$$

$$\frac{p_1}{p_a} = 19.2$$

Test No.	Volume (cm^3)	Computed Dia. (mm)	Mass (gm)	Computed Thickness (mm)	γ_1	Fragment Velocity (m/s)	Corrected Pressure Ratio (p_1/p_a)	$\bar{R}$	$\bar{P}_{s_1}$	$\bar{t}_{a_1}$	$\bar{I}_{s_1}$ (+)	$\bar{I}_{s_1}$ (+)	$\bar{I}_s$ (-)	$\bar{I}_s$ (-)	$\bar{t}_{a_2}$	$\bar{P}_{s_2}$
1	65.5	49.8	19.0	1.0	1.4	68.5	19.2	--		--	--	--	--	--	--	--
2	596.5	104.6	140.0	1.7	1.4	~58.4	~11.6	--		--	--	--	--	--	--	--
3	606.3	105.2	250.0	3.1	1.4	49.4	19.96	0.913	0.188	0.592	--	--	--	--	--	--
4	65.5	49.8	20.0	1.1	1.4	71.3	18.86	0.977	0.215	0.569	0.380	0.041	--	--	1.97	--
								1.154	0.154	0.712	0.474	0.037	--	--	2.02	0.051
								1.24	0.164	0.807	--	0.035	--	--	2.02	--
								1.95	0.142	1.47	0.380	0.027	--	--	3.25	--
								2.66	0.077	2.13	0.474	0.018	--	--	2.68	--
								3.37	0.089	2.85	0.380	0.017	--	--	--	--
								4.08	0.037	3.32	0.474	0.009	--	--	5.10	--
								4.79	0.027	4.03	0.474	0.0063	--	--	5.81	--
5	565.4	102.6	117.5	1.5	1.4	62.6	13.35	0.636	0.289	0.157	0.432	0.069	0.937	0.1072	1.52	0.102
								0.734	0.242	0.183	0.458	0.058	0.925	0.0824	1.53	0.095
								0.783	0.224	0.327	0.406	0.048	--	--	--	--
								1.18	0.163	0.680	0.432	0.033	--	--	2.07	0.060
								1.57	0.132	0.968	0.432	0.026	0.997	0.0540	2.39	0.050
								1.96	0.119	1.44	0.432	0.024	--	--	--	--
								2.35	0.072	1.67	0.471	0.017	0.934	0.0220	3.14	0.027
								2.74	0.060	2.07	0.458	0.013	0.916	0.0183	3.53	--
6	78.7	53.3	28.7	1.4	1.4	~58.4	~29.6	0.785	0.315	0.308	0.365	0.053	0.866	0.0708	1.56	0.102
								0.927	0.245	0.404	0.385	0.045	--	--	1.69	0.076
								0.999	0.287	0.615	0.404	0.048	0.847	0.0574	1.85	0.076
								1.57	0.170	1.0	0.423	0.030	0.843	0.0414	2.25	0.048
								2.14	0.120	1.50	0.442	0.022	--	--	2.81	0.043
								2.71	0.108	2.12	0.462	0.021	--	--	3.44	--
								3.28	0.097	2.60	0.500	0.019	--	--	4.0	0.037
								3.85	0.055	3.17	0.519	0.0093	--	--	4.58	0.027
7	573.5	103.1	310.5	4.0	1.4	~58.4	~28.1	0.488	0.447	0.100	0.361	0.093	0.991	0.1748	1.46	0.205
								0.563	0.365	0.170	0.361	0.079	--	--	1.50	0.183
								0.825	0.270	0.501	0.361	0.051	1.053	0.0793	--	--
								1.13	0.213	0.702	0.371	0.040	0.839	0.0632	--	--
								1.43	0.174	0.962	0.361	0.032	--	--	--	--
								1.73	0.158	1.30	0.401	0.027	0.972	0.0400	2.69	0.058
								2.03	0.109	1.58	0.431	0.020	0.975	0.0302	2.99	0.045
								2.33	0.083	1.85	0.431	0.015	0.961	0.0197	3.29	0.024
8	80.3	53.3	81.9	3.9	1.4	75.9	41.56	0.694	0.403	0.202	0.337	0.072	0.997	0.1122	1.52	0.076
								0.821	0.342	0.320	0.371	0.058	0.943	0.0780	1.65	0.072
								0.884	--	0.506	0.405	--	--	--	1.86	--
								1.39	0.165	0.843	0.422	0.031	0.923	0.0520	2.19	0.039
								1.89	0.124	1.30	0.439	0.025	0.985	0.0413	2.77	--
								2.40	0.103	1.86	0.472	0.024	--	--	3.34	--
								2.90	0.079	2.28	0.422	0.021	--	--	3.76	--
								3.41	0.050	2.87	0.506	0.012	0.972	0.0142	4.30	0.027

Test No.	Volume (cm^3)	Computed Dia. (mm)	Mass (gm)	Computed Thickness (mm)	γ_1	Fragment Velocity (m/s)	Corrected Pressure Ratio (p_1/p_a)	$\bar{R}$	$\bar{P}_{s_1}$	$\bar{t}_{a_1}$	$\bar{T}_{s_1}$ (+)	$\bar{I}_{s_1}$ (+)	$\bar{T}_s$ (-)	$\bar{I}_s$ (-)	$\bar{t}_{a_2}$	$\bar{P}_{s_2}$
9	70.5	51.3	19.9	1.0	1.665	72.3	17.02	1.17	--	--	--	--	--	--	--	--
								1.38	0.146	0.597	0.569	0.040	--	--	2.36	0.056
								1.49	--	--	--	--	--	--	--	--
								2.34	0.084	1.51	0.597	0.024	1.297	0.0359	3.44	0.032
								3.19	0.060	2.33	0.626	0.016	1.312	0.0279	4.27	0.028
								4.05	0.055	3.34	0.626	0.014	1.252	0.0219	5.21	0.030
								4.898	0.039	4.13	0.640	0.010	1.292	0.0120	5.97	0.015
								5.75	0.029	4.98	0.640	0.008	1.317	0.00996	6.86	0.011
10	78.0	52.8	27.6	1.4	1.665	~58.4	~26.8	0.966	0.238	0.381	0.524	0.062	1.174	0.0734	1.81	0.074
								1.14	0.185	0.571	0.476	0.039	1.255	0.0534	2.10	0.045
								1.23	0.204	0.833	0.476	0.043	1.167	0.0534	2.52	0.068
								1.93	0.127	1.29	0.571	0.031	1.105	0.0417	3.0	0.059
								2.63	0.086	1.95	0.571	0.020	1.157	0.0283	3.67	0.040
								3.34	0.076	2.74	0.548	0.016	--	--	4.50	--
								4.04	0.053	3.41	0.619	0.0115	1.164	0.0150	5.12	--
								4.74	0.039	4.07	0.619	0.0099	1.243	0.0100	5.83	--
11	545.7	101.1	285.4	3.8	1.665	57.6	24.26	0.609	0.331	0.125	0.476	0.090	--	--	1.98	0.193
								0.703	0.277	0.213	0.501	0.076	--	--	2.13	0.144
								1.03	0.189	0.626	0.476	0.046	1.206	0.0666	--	--
								1.41	0.163	0.889	0.488	0.041	1.036	0.0548	2.75	0.099
								1.78	0.122	1.23	0.488	0.030	--	--	3.19	0.076
								2.16	0.104	1.63	0.501	0.026	--	--	3.51	--
								2.53	0.077	1.98	0.501	0.019	1.340	0.0281	3.83	0.046
								2.91	0.057	2.32	0.513	0.015	1.352	0.0210	4.19	0.037
12	70.0	51.3	71.3	3.7	1.665	87.5	26.18	0.996	0.268	0.363	0.581	0.075	1.513	0.1102	2.47	0.088
								1.178	0.207	0.533	0.537	0.053	1.515	0.0763	2.64	0.077
								1.27	0.186	0.775	0.557	0.053	1.472	0.0712	2.88	0.066
								1.99	0.142	1.28	0.654	0.037	1.438	0.0576	3.41	0.052
								2.72	0.092	1.94	0.639	0.025	1.573	0.0407	4.12	0.027
								3.44	0.076	2.78	0.726	0.020	1.322	0.0271	4.84	--
								4.17	0.055	3.45	0.726	0.014	1.518	0.0220	5.57	0.029
								4.89	0.043	4.12	0.726	0.010	1.414	0.0153	6.29	0.022
13	758.7	113.2	142.0	1.5	1.665	~61.0	~9.9	0.822	0.201	0.204	0.612	0.066	1.184	0.0945	2.06	0.131
								0.940	0.183	0.314	0.612	0.062	1.158	0.714	2.17	0.095
								0.999	0.159	0.523	0.607	0.055	1.231	0.0780	2.36	0.081
								1.47	0.127	0.785	0.612	0.045	1.182	0.0660	2.67	0.050
								1.94	0.085	1.24	0.581	0.031	1.234	0.0473	3.14	0.053
								2.41	0.071	1.77	0.628	0.025	--	--	3.58	0.035
								2.88	0.058	2.28	0.628	0.019	1.077	0.0220	3.97	0.027
								3.35	0.044	2.67	0.628	0.014	1.179	0.0187	4.52	0.024
14	66.0	50.8	18.7	1.0	1.665	64.2	18.1	1.171	0.168	0.398	0.569	0.047	1.138	0.0578	2.16	0.061
								1.38	0.136	0.569	0.569	0.038	1.260	0.0498	2.36	0.057
								1.49	0.123	1.04	0.541	0.032	--	--	2.87	0.066
								2.34	0.092	1.59	0.569	0.024	1.206	0.0339	3.36	0.047
								3.19	0.056	2.30	0.597	0.016	1.223	0.0219	4.15	0.039
								4.05	0.042	3.41	0.569	0.012	--	--	5.06	--
								4.90	0.032	4.13	0.597	0.010	--	--	5.83	0.021
								5.75	0.028	4.98	0.597	0.006	1.178	0.0080	6.77	0.017

Test No.	Volume (cm^3)	Computed Dia. (mm)	Mass (gm)	Computed Thickness (mm)	γ_1	Fragment Velocity (m/s)	Corrected Pressure Ratio (p_1/p_a)	$\bar{R}$	$\bar{P}_{s_1}$	$\bar{t}_{a_1}$	$\bar{T}_{s_1}$ (+)	$\bar{I}_{s_1}$ (+)	$\bar{T}_s$ (-)	$\bar{I}_s$ (-)	$\bar{t}_{a_2}$	$\bar{P}_{s_2}$
15	573.5	103.1	84.6	1.1	1.665	66.7	12.8	0.762	0.251	--	0.470	0.069	1.341	0.0920	1.90	0.141
								0.879	0.204	0.235	0.533	0.063	1.236	0.0812	2.01	0.110
								0.938	--	--	--	--	--	--		--
								1.407	0.149	0.783	0.542	0.046	--	--	2.58	0.078
								1.88	0.100	1.18	0.542	0.030	1.249	0.0527	2.98	0.061
								2.35	0.079	1.68	0.627	0.023	--	--	3.42	--
								2.81	0.068	2.11	0.627	0.018	--	--	3.92	0.032
								3.28	0.046	2.58	0.627	0.013	1.220	0.0187	4.43	0.023
16	70.5	51.3	15.5	0.81	1.4	~66.0	~18.7	0.957	0.215	0.302	0.418	0.049	--	--	1.65	0.084
								1.13	0.185	0.488	0.418	0.034	--	--	1.84	0.057
								1.22	0.189	0.813	0.418	0.037	--	--	2.16	0.066
								1.91	0.142	1.19	0.488	0.028	0.786	0.0469	2.58	0.042
								2.61	0.087	1.81	0.511	0.018	--	--	3.25	0.032
								3.31	--	2.21	0.488	--	--	--	3.95	--
								4.00	0.053	3.18	0.488	--	--	--	4.65	--
								4.70	0.037	3.95	0.488	--	--	--	5.35	0.015
17	75.1	52.3	30.0	1.50	1.4	65.9	25.5	0.84	0.280	0.245	0.449	0.063	0.855	0.0886	1.59	0.088
								0.993	0.220	0.408	0.408	0.041	0.949	0.0515	1.78	0.060
								1.069								
								1.68	0.156	1.02	0.490	0.030	0.890	0.0429	2.43	0.055
								2.29	0.095	1.59	0.490	0.019	0.920	0.0286	3.00	0.048
								2.90	0.083	2.35	0.469	0.016	0.920	0.0200	3.69	0.045
								3.51	0.074	2.86	0.490	0.011	--	--	4.25	0.027
								4.12	0.039	3.47	0.490	0.0086	--	--	4.86	0.015
18	600.00	104.6	222.0	2.8	1.4	~50.8	~25.3	0.498	0.490	--	0.377	0.087	--	--	1.38	--
								0.574	0.375	0.164	0.368	0.075	--	--	1.46	0.108
								0.843	0.241	0.481	0.384	0.048	0.933	0.0666	1.79	0.104
								1.15	0.218	0.675	0.379	0.042	0.958	0.0659	2.03	0.080
								1.46	0.158	0.941	0.379	0.028	0.937	0.0480	2.28	0.064
								1.76	0.137	1.28	0.409	0.024	0.976	0.0358	2.64	0.050
								2.07	0.097	1.53	0.409	0.019	0.922	0.0222	2.95	
								2.37	0.071	1.84	0.409	0.014	0.991	0.0179	3.22	0.034
19	71.9	51.8	28.2	1.4	1.665	65.6	22.7	1.05	0.217	0.306	0.536	0.057	1.256	0.0661	2.14	0.089
								1.24	0.172	0.510	0.510	0.043	1.284	0.0572	2.35	0.062
								1.34	0.181	0.919	0.562	0.041	1.246	0.0518	2.76	0.087
								2.10	0.142	1.35	0.638	0.033	1.090	0.0357	3.19	0.084
								2.87	0.077	2.04	0.638	0.018	1.205	0.0322	3.88	0.039
								3.63	0.062	2.94	0.638	0.016	--	--	4.72	0.025
								4.39	0.050	3.70	0.638	0.014	--	--	5.39	0.012
								5.16	0.033	4.34	0.638	0.009	--	--	6.25	0.008
20	580.1	103.6	227.0	2.9	1.665	~50.8	~25.3	0.597	0.324		0.491	0.088	1.325	0.1658	1.88	--
								0.689	0.298	0.172	0.491	0.085	1.276	0.1495	1.93	0.135
								1.01	0.219	0.613	0.429	0.047	--	--	2.37	--
								1.38	0.192	0.834	0.460	0.038	--	--	2.64	--
								1.74	0.127	1.15	0.460	0.029	1.313	0.0438	2.97	0.080
								2.11	0.110	1.56	0.466	0.024	1.276	0.0378	3.37	0.066
								2.48	0.076	1.90	0.479	0.018	1.276	0.0275	3.68	0.053
								2.85	0.059	2.25	0.491	0.015	1.325	0.0241	4.06	0.044

REFERENCES

1. H. L. Brode, "The Blast from a Sphere of High Pressure Gas", Rand Corp. Report P-582, 1955.

2. H. L. Brode, "The Blast Wave in Air Resulting from a High Temperature, High Pressure Sphere of Air", Rand Corp. Report RM-1825-AEC, 1956.

3. S. L. Huang and P. C. Chou, "Calculations of Expanding Shock Waves and Late-Stage Equivalence," Drexel Institute of Technology Report No. 125-12, April 1968.

4. R. E. Ricker, "Blast Waves from Bursting Pressurized Spheres", Master's Thesis, Univ. of Illinois, Dept. of Aero. & Astro. Eng., 1975.

5. D. W. Boyer, H. L. Brode, I. I. Glass, and J. G. Hall, "Blast from a Pressurized Sphere", UTIA Report No. 48, Toronto, Canada, January 1958.

6. J. F. Pittman, "Blast and Fragment Hazards from Bursting Pressure Tanks", NOLTR 72-102, U. S. Naval Ord. Lab., White Oak, Md. May 1972.

7. W. E. Baker, Explosions in Air, University of Texas Press, Austin, 1973.

8. W. E. Baker, J. J. Kulesz, R. E. Ricker, R. L. Bessey, P. S. Westine, V. B. Parr, and G. A. Oldham, "Workbook for Predicting Pressure Wave and Fragment Effects of Exploding Propellant Tank and Gas Storage Vessels", NASA Contract Report No. 134906, Southwest Research Institute.

NASA-Langley, 1977 E-9109